Fluid Surface Velocity Measurement using Millimeter-Wave Radar Sensor

Gustav Broman,
Leo Ghatnekar Nilsson

Master's thesis
2022:E46

Lund University

Faculty of Engineering
Centre for Mathematical Sciences
Mathematical Statistics

Centrum Scientiarum Mathematicarum

Master's Theses in Mathematical Sciences 2022:E46
ISSN 1404-6342

LUTFMS-3449-2022

Mathematical Statistics
Centre for Mathematical Sciences
Lund University
Box 118, SE-221 00 Lund, Sweden

http://www.maths.lu.se/

Fluid Surface Velocity Measurement using Millimeter-Wave Radar Sensor

Gustav Broman

gu5860br-s@student.lu.se

Leo Ghatnekar Nilsson

leo.nilsson.96@gmail.com

June 21, 2022

Master's thesis work carried out at Acconeer AB.

Supervisors: Andreas Jakobsson, andreas.jakobsson@matstat.lu.se
Anders Buhl, anders.buhl@acconeer.com

Examiner: Dragi Anevski, dragi.anevski@matstat.lu.se

Abstract

Contactless fluid surface velocity measurements with radar technology presents novel ways of determining fluid flow. The Acconeer A121 sensor is used, which is a pulsed coherent 60 GHz millimeter-wave radar, with high accuracy and low energy consumption. Fluid flow data is obtained from three different sites; in the Acconeer lab, a lab in the UK, and in three sewage pipes of VA SYD. Initially, data from the Acconeer lab is analysed and used to implement the algorithm which later is run and tested on the other data. The basics of the algorithm is creating periodograms by FFT in fast-time and averaging in slow-time dimension. The frequency components are converted to velocities by knowledge of the wave specifics.

The results show that forward and backward flow is easy to measure and distinguish. From Acconeer and UK lab the velocity spectra cohere with the reference velocity data. For the VA SYD sites, the 1500 mm pipe show some peak close to Nivus reference, but the signal strength is weak due to small surface ripples. For the pipe of 750 mm the spectra cohere well with Nivus. The non-stationary flow of the 800 mm pipe seem to cause some error in the measurement.

Keywords: Fluid flow surface measurement, velocity estimation, FFT, fast-time phase change, radar

Acknowledgements

We wish to express our gratitude to Acconeer AB for an interesting project, and especially our supervisor Anders Buhl, who guided us through the process. We are also grateful to our supervisor at LTH, Andreas Jakobsson. Without your guidance, the goal of this project could not have been realised.

We would also like to thank Tomas Wolf, our contact at VA SYD who helped us collect useful data in the sewage environments. Finally, we would like to thank Magnus Larson at the division of Water Resources Engineering for providing us with information about fluid dynamics.

Finally, a sincere thank you to everyone else who helped us during this project, not least our fellow course mates. If you feel that you have contributed to this project, thank you.

Popular Science Summary

Hastighetsuppskattning av vattenytor med 60 GHz radar

Det finns ett stort behov av att förbättra infrastrukturen i vatten- och avloppsnäten globalt. Belastningen på dessa nätverk måste övervakas för att förutspå och undvika skador, översvämningar samt minimera serviceavbrott. Nuvarande lösningar är dyra, vilket öppnar marknadsmöjligheter för mer kostnadseffektiva lösningar.

Traditionellt sett har radar använts i sammanhang för att identifiera större objekt som raketer eller flygplan. Dagens teknikutveckling har möjliggjort för snabba och millimeternoggranna radarsystem som till följd av energisnålheten gör den lämplig för, och används i allt fler batteridrivna produkter inom konsumentelektronik. Kontaktlös mätning av vätskeflöden är en radartillämpning som enkelt skulle kunna ersätta dagens dyra mätningsutrustning med en mindre batteridriven radar. Eftersom den dyra mätutrustningen ofta kräver kontakt med vattnet skulle en övergång till radarövervakade system medföra en förenklad installationsprocess såväl som ett minskat behov av underhåll. Att dagens dyrare mätutrustning är i behov av rengöring märktes i denna studie då det uppmätta flödet i ett dagvattenrör ökade med över 300% efter rengöring till följd av smuts som ansamlas på mätutrustningen, med värden från 0.031 till 0.139 m/s under 2 minuter. Även detta ökar incitamenten ytterligare för en övergång till kontaktlös flödesmätning.

I denna studie används Acconeers A121-radar, en sensor med hög precision och låg energiförbrukning. Flödets ythastighet bestäms med hjälp av den reflekterade signalen och från fasförändringarna kan en hastighet beräknas. Hastighetsuppskattningen görs via de små vågorna/ojämnheterna på ytan som betraktas som små objekt i rörelse. Tekniken fungerar således inte om vattenytan är spegelblank vilket resulterar i en mycket liten eller ingen reflekterad signal tillbaka till sensorn. Implementeringen av en generell algoritm för det totala fluid-flödet är komplicerad då sambandet mellan vattenytans hastighet och det totala flödet varierar och beror bland annat på rörets dimensioner såväl som flödets dynamik. Den algoritm vi utvecklat resulterar i ett spektrum av hastighetskomponenter på ytan, och det är möjligt att uppskatta hur snabbt fluidens yta rör sig. Det här projektet visar på att ythastighetsmätning med Acconeers pulsade radar A121 är genomförbart med den framtagna implementerin-

gen, och är ett kostnadseffektivt system som kan användas i framtiden.

Abbreviations

- ADC - Analog to Digital Converter
- CR - Cross Range
- FFT - Fast Fourier Transform
- DFT - Discrete Fourier Transform
- DR - Down Range
- EM - Electromagnetic
- HWAAS - Hardware Accelerated Average Samples
- IQ - In-phase and quadrature components
- PRF - Pulse Repetition Frequency
- PRI - Pulse Repetition Interval
- PSD - Power Spectral Density

Contents

Chapter 1
Introduction

The current methods of contactless fluid velocity and flow measurements are expensive and often require different specifics of the fluid, such as particles for the signal to reflect on. In the global perspective of improving the infrastructure of sewage systems and mitigating damages and service maintenance, it is desirable to supervise different fluid flows. Combining an efficient way of contactless fluid velocity measurement with this infrastructural improvement has a big market potential.

The publicly-traded company of Acconeer provides the pulsed coherent radar sensor A121, a sensor with high accuracy and low energy consumption. The energy efficiency is especially useful for battery driven electronics. Using the 60 GHz band-width, i.e., a millimetre-wave pulse, the sensor returns data as complex numbers packaged in the fast-/slow time (sweep-/frame) dimension.

It is the purpose of this project to implement a fluid surface velocity algorithm for the Acconeer A121 sensor. The implementation is based on fast-time phase change of the wave and requires surface waves/ripples structure for reflection of the signal. These small surface irregularities are seen as moving objects, from which we determine a phase shift of the wave, i.e., a velocity.

The measurements and data collection of this project are done in three settings; the Acconeer lab, a lab of a company in the UK, and on three sites of VA SYD which are called `GYGK_K1500`, `TULK_750`, and `TUAS_800`. The number describes the diameter of the sewage pipe in mm. For `GYGK_K1500`, the amplitude of the return signal is weak which results in a less protruding peak in relation to the background noise. This is referred to as a low signal-to-noise ratio, SNR. The peak that is obtained however matches the reference velocity of the Nivus measurement, a reference that is provided on site by VA SYD. The `TULK_750` pipe shows good spectra for the fluid flows with Nivus reference slightly higher than the centre of the spectrum peak. This is expected since Nivus measures just below the surface where the velocity is higher than the surface. For `TUAS_800` the flow is non-stationary which for some measurements are problematic. In the Acconeer lab and the UK lab the spectra are ideal with

reference value matching. In the Acconeer lab forward and backward flows are measured and from the spectra it is easy to determine which flow is in what direction.

The algorithm of the signal processing is to construct the power spectral density (PSD) estimation by the squared absolute value of the fast Fourier transform (FFT) in the sweep dimension, averaged in slow-time (mean over frames). This is done for the complex valued signal data returned by the A121 sensor. The frequency bins are then converted to velocities by knowledge of the pulse specifics.

The structure of this report is as follows. Chapter 2 introduces relevant theory regarding general-/the Acconeer radar, periodogram estimation, the velocity estimation, and different surface velocity profiles. In appendix A, some basics on electromagnetic waves are found. In chapter 3, the methodology of sensor setup, data collection and signal processing is described. The results of the measurements are found and discussed in chapter 4. Finally, some conclusions of the project measurements are found in section 5.1.

Chapter 2

Theory

For basic electromagnetic wave theory the reader is referred to the appendix A.

2.1 Radar

Radar is an acronym for Radio Detection and Ranging. Modern radars however can detect both the relative distance as well as velocities or classifying objects. It is an electrical system that transmits electromagnetic waves and detects the reflected signals from a certain region. Figure 2.1 shows an example of the major elements involved in a radar following the signal from the transmitter all the way to the signal processor.

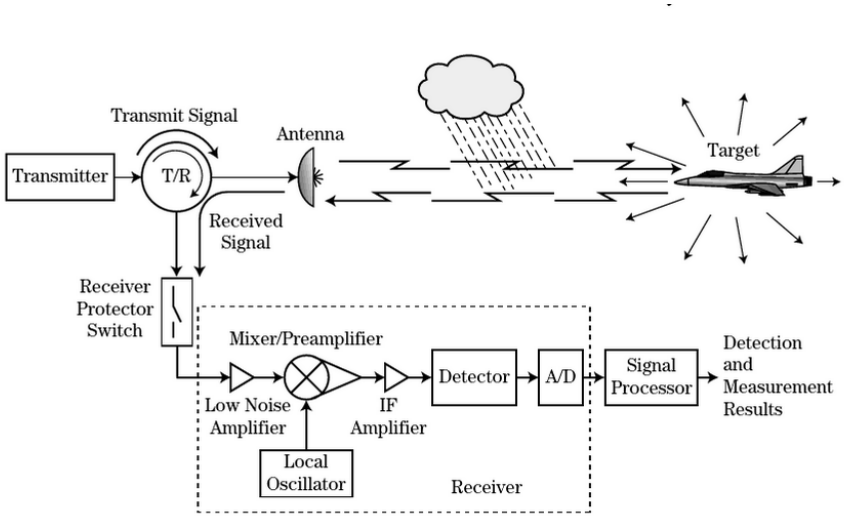

Figure 2.1: The figure represent a schematic example view of a radar system (1).

Although this is just an example of a radar system, all radars must at least include a transmitter, receiving antenna, and a signal processor (1).

The part that generates the EM-wave is the transmitter, this signal is generated and sent out through an antenna. In figure 2.1, there is a T/R switch connected to the antenna that makes sure it can be attached to both the transmitter and receiver preventing them from any direct interaction. Another common way is to skip the T/R switch and have two separate antennas for transmitting and receiving. The received signal from any reflecting target is then input to the receiver circuits marked with a dashed rectangle in figure 2.1. In this part, the radio signal is amplified and converted to an intermediate frequency and then it goes through an analog-to-digital converter (ADC) before it reaches the signal processor (1).

When operating with radars there are often two spatial dimensions of interest. Cross-Range (CR) and Down-Range (DR) demonstrated in figure 2.2.

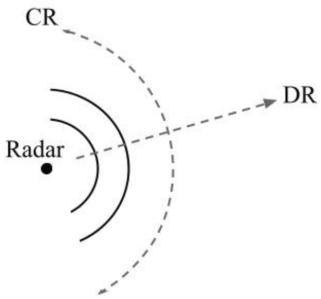

Figure 2.2: The figure illustrates the CR- and DR-directions for a radar.

DR is the dimension in which the radar signal propagates in through time whereas the CR is the directions normal to DR and makes out the 'wave-front' of the signal. A 'time of flight' radar system can therefore only detect movements in the DR direction.

2.1.1 Pulsed coherent radar (PCR)

A pulsed radar transmit short pulses of EM-waves through the transmitting antenna during a short period. At this time the receiving antenna is isolated and no reflected signals can be detected during this time. In between the transmitted pulses the receiver connected to the antenna detects possible reflected signals. The interval between two pulses is often referred to as *pulse repetition interval* (PRI) and the number of cycles per unit time is called *pulse repetition frequency* (PRF) and is simply the inverse of the PRI. The passage of time for a pulsed radar is represented in figure 2.3.

EM-waves are said to be coherent if the phase relationship is constant between pulses. One way to accomplish this is to have a coherence oscillator used as a reference. The pulses then consist of partial sections of this continuous oscillation so that every pulse is in phase with the reference (2). This can be visualized in figure 2.4.

The top signal is a stable continuous oscillation used as the reference and the middle signal is the coherent since pulses are made based on the phase of the reference oscillation.

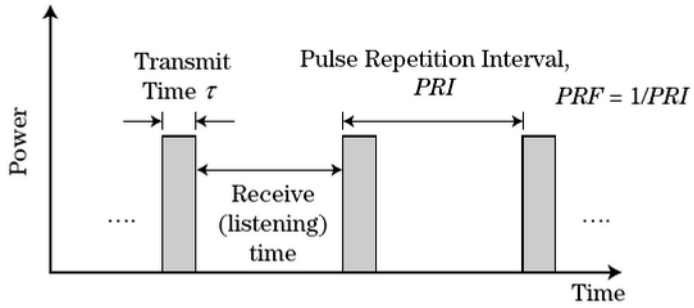

Figure 2.3: A block schema over the pulsed radar over time ([1]).

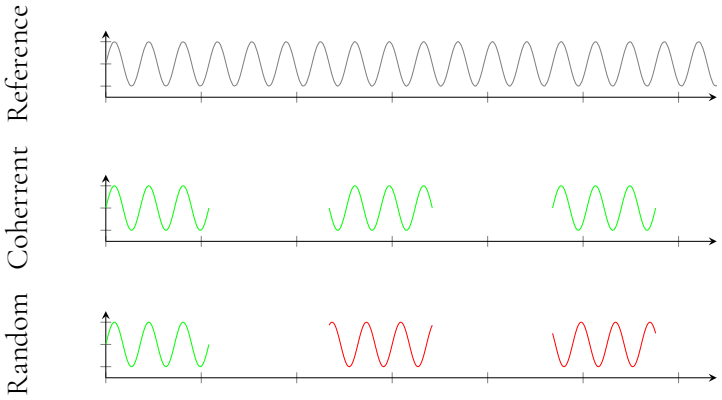

Figure 2.4: The figure illustrates how a pulsed coherent signal (middle) can be made using a reference (top) and a random pulsed signal (bottom). The green pulses are in phase with the reference signal.

Pulsing with random phase like in the last signal is therefore a non-coherent pulsed signal.

2.2 Acconeer Radar Sensor

This project is based on the Acconeer A121 sensor which is a pulsed coherent radar operating at 60 GHz, resulting in a wavelength of 5 mm in free space which gives a resolution of approximately 2.5 mm. The radar system is a 'time of flight' system meaning that the time between the transmitted signal and received signal is measured and used to calculate the DR distance to objects.

2.2.1 Configuring the sensor

There are multiple settings that can be tuned in order to optimize the sensor performance for specific use cases and requirements. First of all the *pulse length profile* (Profile) specifies the transmitted pulse lengths. Shorter pulses provides higher distance resolution and longer pulses reduced the depth resolution. On the other hand short pulses results in a reduced SNR (signal-to-noise ratio) compared to longer pulses so there is a trade-off between SNR and

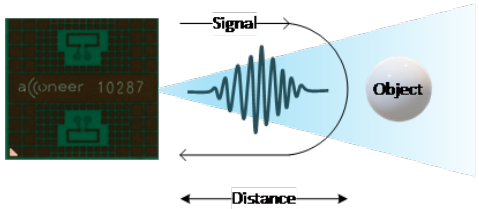

Figure 2.5: A visualisation of Acconeer's time of flight radar system (3)

depth resolution. Different profiles also result in different 'leakage' between the transmitter and the receiver. This is the process where the transmitted signal goes directly from the TX-antenna (transceiver) to the RX-antenna (receiver) without reflecting at an object. In addition to the profile there are two other parameters available to optimise signal quality namely averaging and gain,

- *HWAAS* (Hardware Accelerated Average Samples) is related to the number of pulses averaged in the radar for one data point.
- The gain of the amplifiers in the sensor can be adjusted so the ADC is not saturated and that the signal is separated from noise.

When using the Acconeer sensor one will be acquainted with *sweep* which is defined as a distance measurement range. Hence every sweep consist of one or several distance sampling points. The time between each sweep sample T_s is configurable through the *sweep rate* defined as $f_s = 1/T_s$.

Additionally there is another term that you can set, namely the number of *sweeps per frame*. A *frame* is a container that stores all the data for all distance points and the number of frames together with the other mentioned parameters can be set in the Sparse-IQ GUI (graphical user interface) in the appendix (figure B.1).

2.2.2 The sparse IQ service

For the setup of this project, the signal is sampled using the Acconeer sparse IQ-service. The IQ-service provides data in complex value form in the carthesian coordinate system according to figure 2.6 (3).

IQ-signals or Quadrature signals are often used in radio frequency applications. Two sinusoidal signals with the same frequency shifted in phase by 90 degrees, is said to be in 'quadrature'. By convention the I-signal and Q-signal is cosine- and the sine-wave respectively.

From (3) we learn that having the phase of the signal response available makes it possible to perform accurate measurements. This is seen in figure 2.7 where an object is moving radially towards the radar. The envelope signal (where only the amplitude is available) varies only slightly, while the value of the coherent signal at a fixed time delay varies substantially.

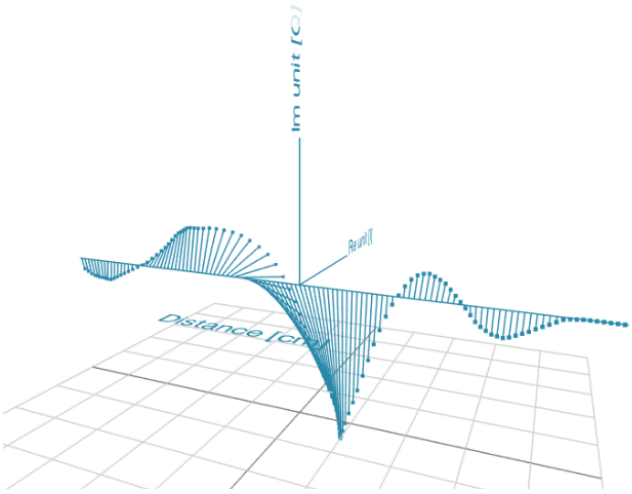

Figure 2.6: Output from the IQ service in Acconeer Exploration Tool (3).

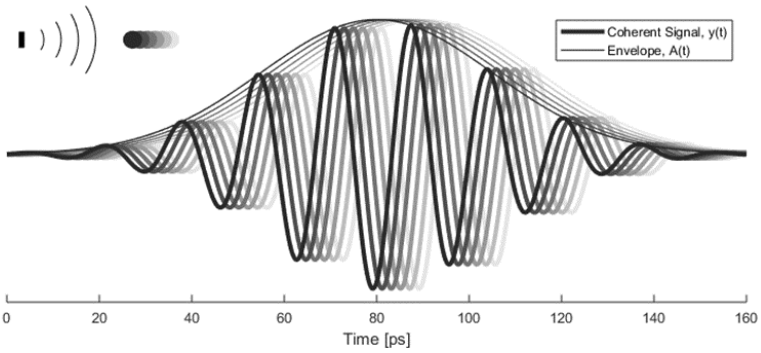

Figure 2.7: Illustration of envelope and phase change of a received pulse for a reflection from a moving object, what is returned from the sparse IQ Service in Cartesian form. (3)

This change will be present in the phase of the data from the sparse IQ service which we use for the analysis and conversion from time to frequency domain and further to a velocity.

For the sparse IQ service the incoming wavelet is sampled every ~ 2.5 mm, which makes it ideal for measuring moving objects. Figure 2.8 illustrates how the sparse IQ service samples the reflected waves of a moving object.

As seen in figure 2.8, the three different blue coloured waves are from different time points, where the darkest one is the most recent (present), and the faded ones are from the past. For every point in time, a sample is taken at the sampling point(s).

The bottom plot lays out the sampled points over a time scale. In this simple example, the object moves with a steady velocity. As such, over time, the samples will reconstruct the incoming wavelet, which the orange line illustrates.

For the sparse IQ service, the incoming data consists of frames, where every frame has a number of sweeps N_s which are sampled after each other. Every sweep consists of one or several (sparse) sampling points in distance as configured. The time between sweeps T_s is

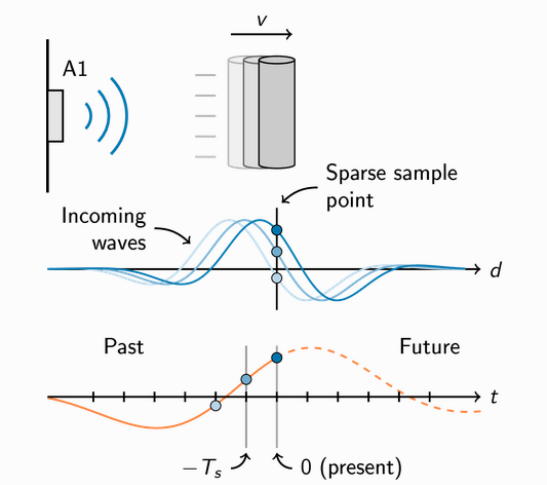

Figure 2.8: An illustration of how the sparse IQ service samples reflected waves from a moving object. The incoming wavelet is sampled every ~ 2.5 mm. (4)

varying in the configuration in the setting of the sweep rate $f_s = 1/T_s$ (4). This sparse data sampling is illustrated in figure 2.9. The sweep-/frame-dimension are referred to as the fast-/slow-time dimension respectively.

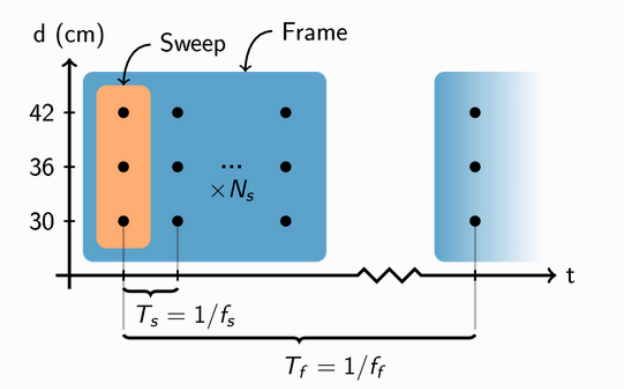

Figure 2.9: An illustration of the sparse data frames consisting of a number of sweeps (4). The sweep-/frame-dimension are referred to as the fast-/slow-time dimension respectively.

2.2.3 Mounting of the A121-sensor

In the lab environment of Acconeer and UK, the Acconeer radar A121 sensor is integrated on the evaluation kit with a XC112 (the card on the raspberry-pi) and a XR112 (the card on which the sensor is mounted). This integration is mounted on a holder which is called LH112 with two positions D1 and D2 for placing a focusing lens. At the sites of VA SYD, the sensor is integrated on a XM122 and XB122 which is mounted on the holder LH122 instead. These

evaluation kits are not further described in this report.

The two lenses used in this project are the HBL (hyperbolic lens) and the FZP (Fresnel zone plate). Pictures of these two lenses are seen in figure 2.10 (number 2 is HBL, and FZP number 3). These two lenses focus the transmitted signal from the A121 sensor.

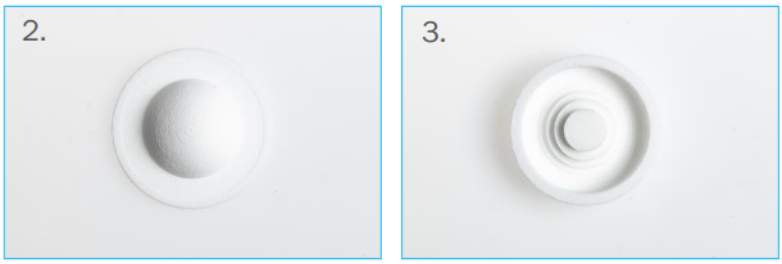

Figure 2.10: The two focusing lenses used in this project, the HBL-lens (number 2) and the FZP-lens (number 3) (5).

The different lens mounting positions D1 and D2 on the LH112 holder are seen in figure 2.11. These positions are the same on the LH122 holder (5). The focusing specifics of these two lenses mounted on the LH112 and LH122 respectively, are described in figure B.6 and figure B.7 in appendix B (5). The numbers are not measured in this project, but are done by Acconeer in lab environment.

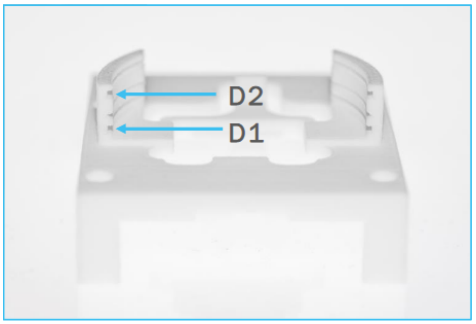

Figure 2.11: Picture of the two lens-mounting positions D1 and D2 on the LH112 holder. The position settings are identical on the LH122 holder. The different positions cause different specifications on the transmitted signal. (5).

The sensor signal dispersion angular dependence is shown in figure 2.12. The notation of E-plane and H-plane angles is used. For this image the default dispersion is shown, i.e., no lens focusing. That makes the E-/H-plane angle to be 40° and 80° respectively. This is for the half power beam width which is the angle in which relative power is more than 50% of the peak power, in the effective radiated field of the antenna.

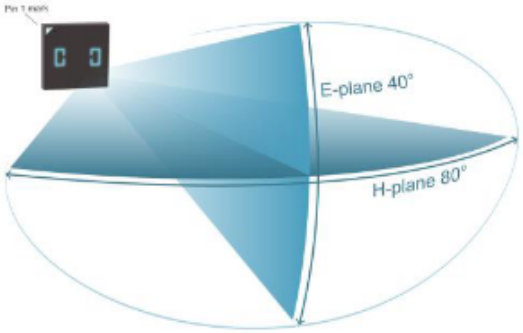

Figure 2.12: The sensor signal dispersion angular dependence in default mode, i.e., with no lens used. That makes the E-/H-plane angle to be 40° and 80° respectively (5).

2.3 Fourier transforms and power spectral density (PSD)

From the received signal one can analyze the phase shift and identify the power located at a specific frequency by Fourier transforming the data. This method gives how much spectral content that is located at a certain frequency and this frequency can later on be transformed into a velocity.

The Fourier transform of a continuous function $y(t)$ is defined as (6)

$$\mathcal{F}(y(t))(f) \equiv \int_{-\infty}^{\infty} e^{-2\pi jft} y(t)\, dt. \tag{2.1}$$

For a function $y(t)$ only defined on $t \in [0,\ T]$, the equation above is transformed into

$$Y(f) = \int_{0}^{T} e^{-2\pi jft} y(t)\, dt. \tag{2.2}$$

For discrete values of N samples of the function at $t = k\frac{T}{N}$, $k = 0, \ldots N-1$ the integral is approximated to the sum of

$$Y(f) \approx \sum_{k=0}^{N-1} e^{-2\pi jfkT/N} y(kT/N)(T/N). \tag{2.3}$$

Specializing the relevant frequencies to $f = m/T$, $m = 0, \ldots N-1$, we find that

$$Y(m/T) \approx \frac{T}{N} \sum_{k=0}^{N-1} e^{-2\pi jmk/N} y(kT/N), \quad y_k = y(kT/N). \tag{2.4}$$

This makes the discrete Fourier transform (DFT) of a sequence y_k to be

$$Y_m = \mathrm{DFT}(\{y_k\})(m) \equiv \sum_{k=0}^{N-1} e^{-2\pi jmk/N}\, y_k, \tag{2.5}$$

up to the normalizing constant $\frac{T}{N}$. The data processing algorithm of this DFT operation is called fast Fourier transform (FFT).

For constructing an estimation of the power spectral density (PSD) of the signal, the periodogram is calculated by the squared absolute value of the DFT, i.e.,

$$\frac{1}{N}\left|Y_m\right|^2 = \frac{1}{N}\left|\sum_{k=0}^{N-1} e^{-2\pi jmk/N}\, y_k\right|^2. \tag{2.6}$$

This makes for a spectral representation of the measured frequencies of a received signal (7). An example figure of the periodogram for two sinusoidal functions presented in figure 2.13. The two functions have different frequencies (30, 50) Hz and different amplitudes. Code for creating the plot is presented in appendix B, figure B.2.

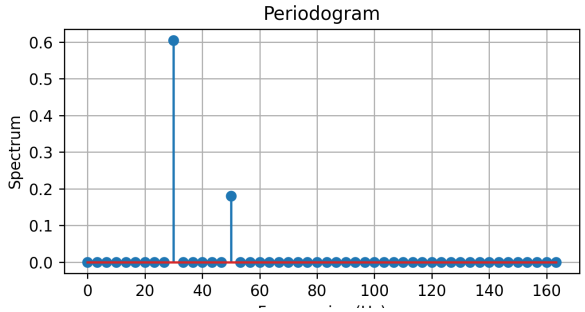

Figure 2.13: An example figure of the periodogram for two sinusoidal functions with different frequencies (30, 50) Hz and different amplitudes. Code for creating the plot is found in appendix B.

2.4 Velocity estimation

The general radar system calculate a velocity through the Doppler frequency shift. In presence of a target moving DR with a radial velocity v_r (between the transmitting object and the observer), due to the Doppler phenomenon, the echoed signal will be shifted in frequency. In a monostatic radar system (transmitter and receiver is at the same location), the distance travelled by the EM-wave is twice the distance between the target and sensor. Hence, the Doppler shift travelling to and from the target becomes

$$f_D = -f\frac{2v_r}{c}. \tag{2.7}$$

The convention that the velocity v_r is defined to be positive when the radial distance increases is used (8). However, finding the Doppler frequency for pulsed radar systems is more complex. According to (9), the typical pulse length (transmitting time) of a pulsed system is usually some nanoseconds, resulting in that only a small fraction of a complete Doppler frequency cycle is contained within a pulse. Thus, the frequency domain solution will contain spectral leakage in the Doppler spectra and result in false velocity calculations. To solve

this, one popular technique often used is to collect consecutive pulses and reconstructing the Doppler frequency (9).

However, measuring a fluid surface velocity is not possible with the Acconeer 60 GHz radar since the the frequency is to way to high compared to the expected flow velocities. The solution for this project is instead to use an easier version of the pulsed Doppler using only the phase difference between sweeps. We refer to this as the fast-time phase change.

A received signal has to be sampled with a frequency at least twice the frequency of the sampled signal according to Nyquist criterion to avoid aliasing, i.e.,

$$f = \frac{f_s}{2}.$$

This makes for a theoretical maximum velocity that can be determined based on the sweep rate,

$$v_{max} = \frac{c \cdot (f_s/2)}{2 \cdot f} = \frac{c \cdot f_s}{4 \cdot f} \approx 0.00125 \cdot f_s \ [m/s] \tag{2.8}$$

where f is the frequency of the radar wavelets and f_s is the sweep rate. Note that this is the maximum velocity to/from the sensor in the DR direction.

2.5 Surface velocity profiles

In this report only free surface fluid flows are measured which are also referred to as open-channel flows. Additionally, the measurements are done in circular or rectangular pipes.

In a plot from (10), we see in figure 2.14 how the surface velocity field in the longitudinal and transversal direction vary. Note that the velocity v increases from $v_{min} = 0$ at the pipe walls to v_{max} in the middle.

Because of surface velocity components varying from $[v_{min}, v_{max}]$ it is expected that all these components are represented in the spectrum when conducting the measurements and forming the periodogram.

We note that the plot in figure 2.14 is for a rectangular channel. The surface velocity profile for a circular pipe is however somewhat similar. More in-depth research regarding fluid profiles for circular/rectangular pipes are left as future topic research in section 5.2.

Research conducted by (11) show that the position of the maximum flow velocity is found just below the fluid surface and varies with the fluid depth. Figure 2.15 also shows that the maximum velocity gradually increases with the flow depth. It is seen in the figure how the fluid velocity varies in the depth of the open channel flow for a circular pipe. The max velocity is found just below the surface.

More and deeper theory in the regards of different fluid mechanics is disregarded henceforth in this report.

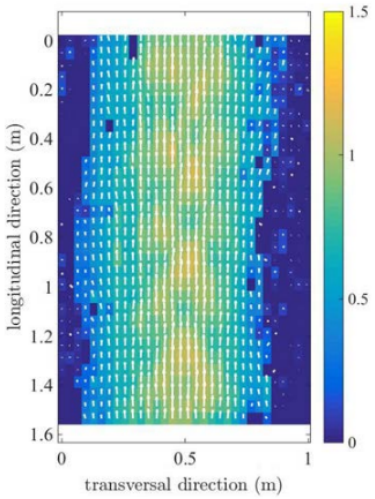

Figure 2.14: A plot from (10) of how the surface velocity field in the longitudinal and transversal direction vary. Note that the velocity v increases from $v = 0$ at the pipe walls to v_{max} in the middle.

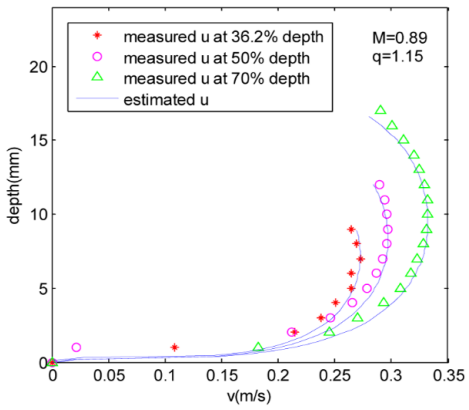

Figure 2.15: From (11) it is seen that the depth-wise fluid profile for a circular open channel flow. The max velocity is found just below the surface. The maximum velocity gradually increases with the flow depth.

Chapter 3
Methodology

3.1 Sensor Setup

In this project, the fluid surface velocity is measured with a set up demonstrated in figure 3.1.

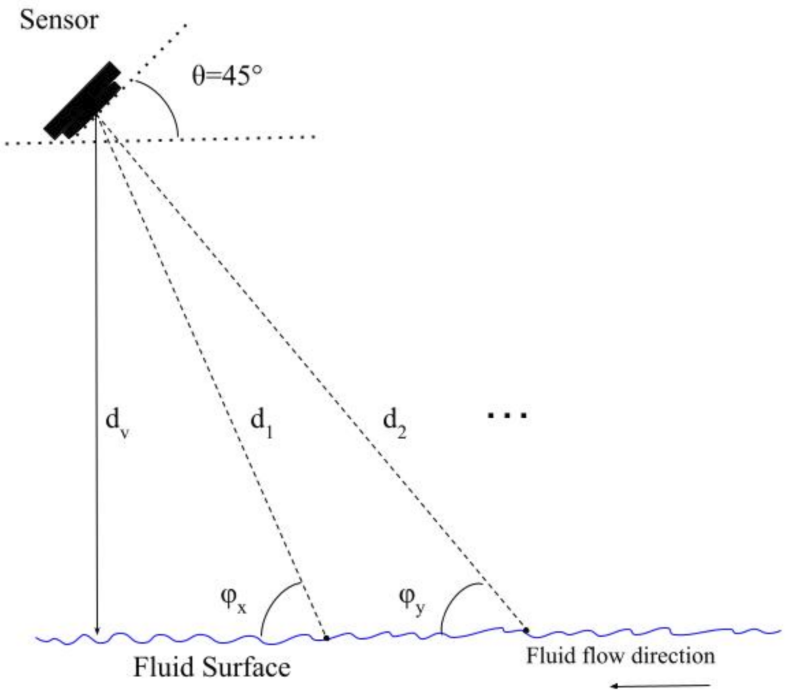

Figure 3.1: The figure represents the desired setup of the sensor above a open channel flow fluid surface, measuring the 'backward' flow.

The sensor is placed above the fluid surface with an angle chosen to be 45° since it is a trade-off between receiving reflections and measuring the horizontal velocity component. We define the direction of fluid flow as 'backward' when measuring against the flow as in figure 3.1 and 'forward' when the flow is in the opposite direction (fluid moving away from the sensor).

Knowledge about the distance d_v vertically down from sensor to fluid surface makes it possible to calculate the angle of incident for different distance points by

$$\varphi = arcsin(\frac{d_v}{d_x}). \tag{3.1}$$

Assuming that the fluid level is stationary compared to the frame rate we can neglect the vertical velocities of the surface since they cancel out each other. Hence the resulting velocity measured will be the radial component of the horizontal fluid velocity resulting in a velocity as,

$$V_{fluid} = V_{measured}\frac{1}{cos(\varphi)}. \tag{3.2}$$

The different configuration parameters of the sparse IQ-service are dependant on which flow you are about to measure. The motivation of the parameters is as follows. Pulse length profile is selected so that the SNR is maximised without including direct leakage in the sweep. The number of sweeps within a frame determines the frequency resolution (which is later converted to a velocity) and is therefore selected to be large (in our case maximum of 256). The sweep rate is set according to equation 2.8 so that the maximum measurable velocity is not exceeded and finally, in order to reduce noise, the *HWAAS* is set to be fairly high to average over more pulses for each data point.

3.2 Data collection

Data are obtained and analyzed from three different settings; in Acconeer lab environment, in a lab environment at a UK-site (similar to our lab setup), and at three sites of VA SYD. For simplicity and structure, results will be presented in this segmentation.

3.2.1 Acconeer lab environment

The initial process of this project was to obtain fluid flow data to identify relevant characteristics and to initiate the analysis of the data. In our lab environment we established a flow device consisting of a PVC-tube through which a water could flow via a garden hose. The whole flow-device could be tilted with some styrofoam discs to achieve different flow velocities and fluid levels in the pipe. In figure 3.2, the setup in the lab environment is shown. In the middle of the PVC-tube a window was cut at which we measure the signal with the A121 radar which is connected with some evaluation kit on a Raspberry Pi. The data is transferred via Wi-fi.

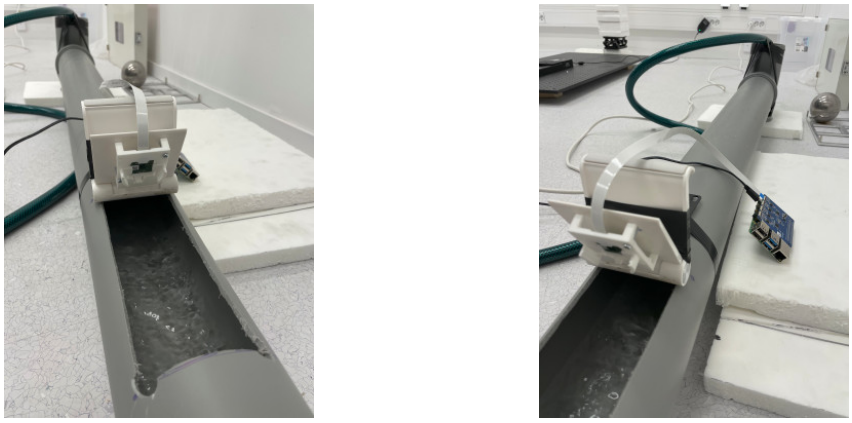

Figure 3.2: The figure shows two images of the setup in our lab environment with water flowing. The sensor is angled at approximately 45° and is connected with some evaluation kit to a Raspberry Pi, described in section 2.2.3.

Additional measurements were performed having the sensor further away from the water surface as represented in the figure 3.3. To the left in the image some pink styrofoam discs are seen, on which the sensor is mounted upon. Doing this enables the use of a different profile.

Figure 3.3: The figure shows the sensor further up above the water surface compared to the setup in figure 3.2. An increased distance from sensor to water surface enables the use of a different profile setting.

Different surface flow velocities were measured in this laboratory setup to analyze the data and the signal response. The exact surface velocity the flows are not determined due to the lack of reliable methods. However, the method of estimating the true velocity is to film the event of dropping a small floating device in the 'window' of the PVC-tube and measuring the time and distance travelled from the window to a small peep-hole ~0.8m along the tube. This is done by a mobile phone camera and an Apple watch as in figure B.5 in appendix.

The measurement of forward and backward flow was also conducted, having the same water flow through the pipe, but turning the sensor around.

3.2.2 UK lab environment

From a company based in the UK we receive flow data from their lab environment similar to our own. With exact water dimension measurements and water volume, the average water speed can be determined. The setup is shown in figure 3.4. As in our lab environment, the sensor is mounted on some evaluation kit connected to a Raspberry Pi.

Figure 3.4: The figure shows the setup of the lab environment at the UK site used to collect flow data with reference velocity data.

For the initial measurements from their setup a rectangular open channel pipe was used. If required a circular pipe could be inserted into the channel for circular open channel flows. The setup for the rectangular open channel pipe is shown in figure 3.5.

Figure 3.5: Water flow in the rectangular open channel on UK lab site.

The sensor casing was angled at ~45° towards the water surface, the same as in Acconeer lab environment. The reference flow rate was measured with a magnetic flow meter in the

return pipe beneath the flow rig. Note that it is therefore a velocity for the entire fluid flow, not just the surface velocity.

3.2.3 VA SYD site

The further data collection was done on three different sites of VA SYD, with reference data of the velocity available. The sensors were installed in casings which were submerged in the sub-ground level sewage pipes. With a ~45° angle above the fluid level the measurements were done. A picture of the installation at one of the sites is shown in figure 3.6. The installations are similar in all of the three pipes.

Figure 3.6: A picture of the installation of the sensor fluid flow measurement device at the 800 mm pipe `TUAS_800` site of VA SYD. The installations are similar in all of the three pipes.

The measurements were conducted at three different sites which are named `GYGK_K1500`, `TULK_750` and `TUAS_800`, where the number specifies the diameter of the pipe in mm.

For the `GYGK_K1500`-pipe the flow velocity was relatively low with almost no surface ripples. This makes the return signal low relative to the noise. Both `TULK_750` and `TUAS_800` had higher velocities and more surface ripples, which generate stronger return signals. For `TUAS_800` there was some water pumping in the system causing non-stationary water flows, with varying velocities and varying water levels. This has implications for the interpretation of results, see section 4.

The reference data from the sites of VA SYD were obtained from the technology of Nivus GmbH. They provide a flow measure device installed at the bottom of the pipe. The water is segmented into 'gates' and in every segment, the velocity is measured by the Doppler effect of particles in the water. Used as reference in this project is the velocity in the 'last gate', i.e., the water layer closest to the surface.

3.3 Signal processing

Converting the signal to a velocity is done in steps as described in figure 3.7. The data is sampled and stored as complex numbers in the sweep-frame packaging of figure 2.9. Then for a frame, all the sweeps for a specific distance is carried as input to the PSD. For this distance the FFT is done in fast-time dimension and the periodogram is calculated as per section 2.3 taking the squared absolute value of the Fourier transform. The PSD estimation is then done by averaging these periodograms in slow-time, i.e., in the frame-dimension.

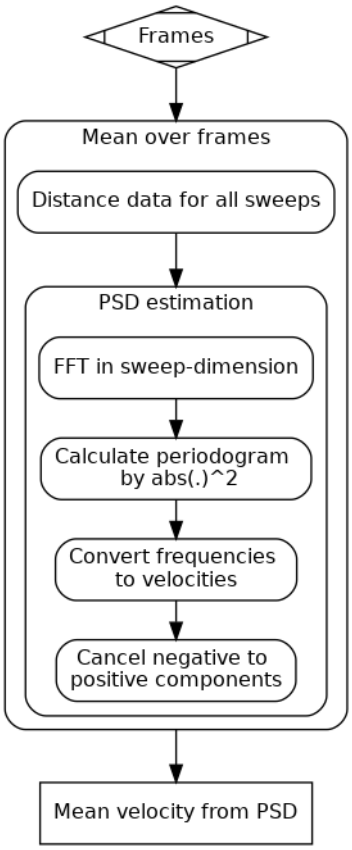

Figure 3.7: Schematic overview of the signal processing for the surface velocity measurement algorithm.

Finally, the frequencies are converted to velocities by

$$x_{vel} = x_{freq} \cdot \lambda_{eff} \cdot C_{\varphi} \tag{3.3}$$

where x_{freq} is the frequency x-axis of the PSD and

$$\lambda_{eff} = \frac{c\,[m/s]}{2 \cdot 60 \cdot 10^9\,[s^{-1}]} \tag{3.4}$$

representing the effective wavelength (half the wavelength) and finally

$$C_{\varphi} = \frac{1}{cos(\varphi)} \tag{3.5}$$

is the compensation for the angle of incident for the reflected wave. Converting the PSD to a mean velocity is a bit tricky since the spectrum will contain low-frequency components that is considered 'fake' since they correspond to slow phase-shifts or static reflections. Possibly these are due to small movements vertically or leakage in sensor which are cancelled out yielding a more understandable spectrum (to be shown in figure 4.2). Since the x-axis of the spectrum is symmetric the negative and positive side can be cancelled out component-wise by removing the lowest value (out of the positive and corresponding negative) from both of them. Finally the zero-component is set to zero since this would correspond to reflections of static objects. From this modified spectrum the surface mean velocity is calculated through mean averaging, as described in section 3.3.1 and in equation 3.6.

This algorithm is done for multiple distance points of the signal. Since the vertical distance from the sensor to the fluid surface d_v is known, the angle of incident for the distance d in the trajectory of the sensor is known and we can use multiple distance in the velocity estimation.

3.3.1 Mean surface velocity

After forming the periodogram with the signal processing methods of section 3.3 we wish to find the mean surface velocity of the flow. Based on section 2.5, figure 2.14 and the periodogram plot of figure 2.13 we form the mean by taking the weighted mean of the amplitude of the signal multiplied with the corresponding x-value velocity, i.e.,

$$v_{mean} = \frac{1}{\sum_{i=0}^{N} y_i} \sum_{i=0}^{N} y_i x_i \tag{3.6}$$

Chapter 4
Results and discussion

The measurements of this project are done in three different settings as described earlier. For clarity and transparency the results will be presented in the same sectioning as before, i.e., the Acconeer lab, UK lab, and site of VA SYD.

First some results are presented for the step-wise signal processing part of this project. The data is from a measurement in the Acconeer lab. The left hand side plot in figure 4.1 show the first 40 sweeps for some frame in complex value form. To the right is the FFT of the same data, with a clear peak at the zero Hz frequency.

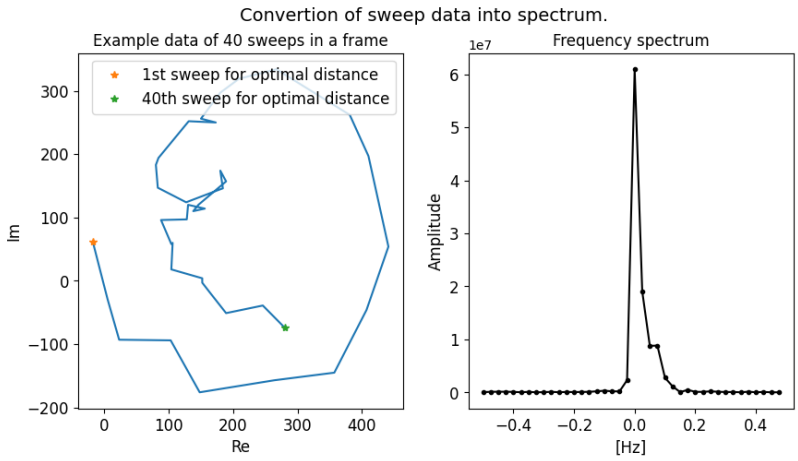

Figure 4.1: The left plot shows the first 40 sweeps for some frame, represented in complex value form. The right plot shows the FFT of the same data, with a clear peak at the 0 Hz frequency.

Figure 4.2 is an example of processing for a measurement. The dotted line shows the PSD estimation of the data, i.e., the squared absolute value of the FFT (the periodogram)

averaged over all the frames. The blue line in the plot shows the same procedure, but after the PSD estimation, the negative velocity components have been removed from both the negative and the positive x-axis. This signal processing step does not affect the conversion into a mean velocity but makes it easier to visualize the power spectrum mean of 0.439 m/s. This is because of the symmetry of the noise frequencies around the x-axis.

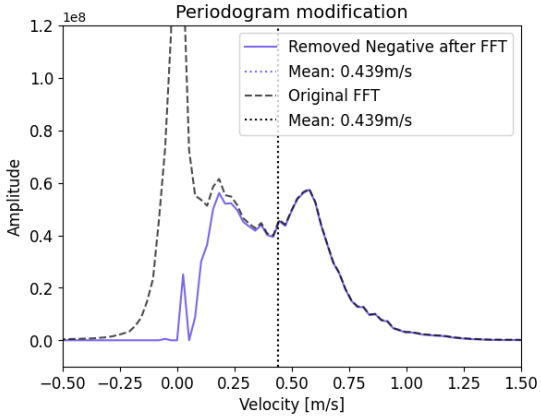

Figure 4.2: The dotted line shows the data after the squared absolute value of the FFT, averaged over all the frames. For the blue line the negative velocity components have been removed from both the negative and the positive x-axis. The mean velocity is calculated to be 0.439 m/s.

4.1 Acconeer lab environment

Figure 4.3 illustrates how a spectrum looks for a measurement done in the Acconeer lab with the three distances closest to the 45° angle of incident, i.e., 51°, 46° and 43°. Note the mean values for the respective distance and the reference value measured according to section 3.2.1.

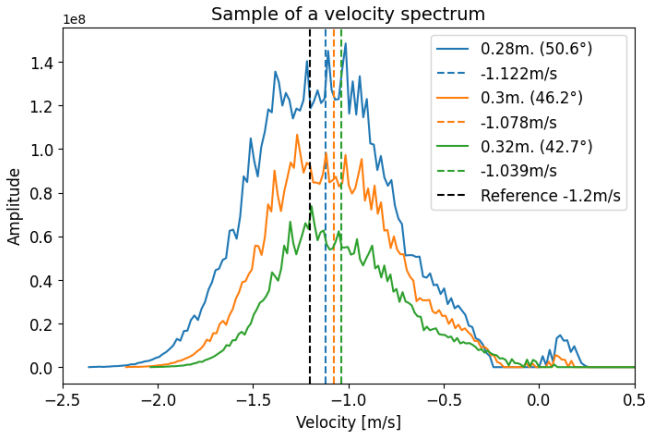

Figure 4.3: The plot illustrates how a spectrum looks for the three distances closest to the 45° angle of incident, i.e., 51°, 46° and 43°, with a vertical line for the mean value computations and the reference mean surface velocity.

The spectra in figure 4.3 show that each PSD cohere for each distance around the 45° angle distance, which is in accordance with what one could assume. Hence, it is independent of selected distance point and is rather a trade-off between the reflected signal strength and how much of the horizontal component that is measured. The latter is preferable since it's reduces the noise and is multiplied with a smaller constant compensating the angle of incidence. It is also clear that the basic assumption that the conversion from received signal to velocity spectrum results is correct. The spectra for each distance is centred around some mean value of the surface velocity.

Figure 4.4 show four different spectra, the 45° angle from four different measurements with different surface velocities. The increasing velocities are obtained by increased inclination of the pipe, and it is clear that the spectra is shifted towards higher velocities. Potential variations in PSD could be due to a wrongly measured distance (or fluctuating water surface) down to the surface hence compensating for an angle that is incorrect.

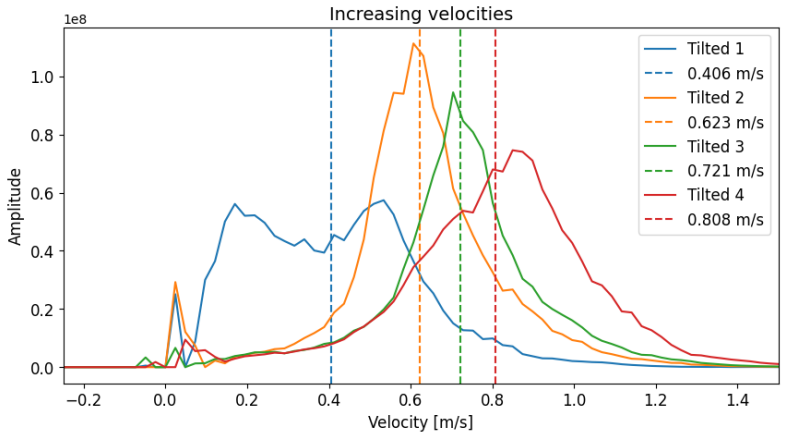

Figure 4.4: Plot of the measurement for the 45° angle for four different water flow velocities. The dashed lines are the calculated mean surface velocity of the respective measurement.

Furthermore the subplots presented in figure 4.5 are the same tilted measurements as in figure 4.4, but with the three distance points closest to the 45° angle. An approximate measurement of the reference surface velocity is done and represented in the plot.

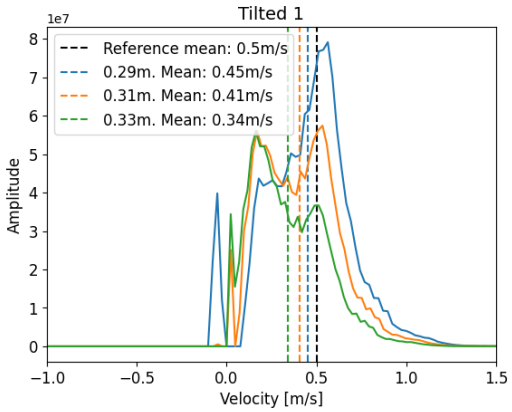

(a) Tilted 1, reference mean surface velocity of 0.5 m/s.

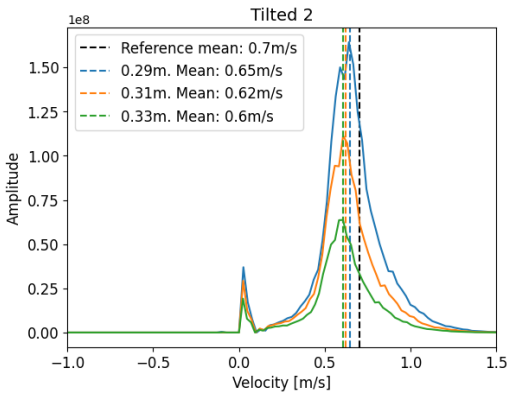

(b) Tilted 2, reference mean surface velocity of 0.7 m/s.

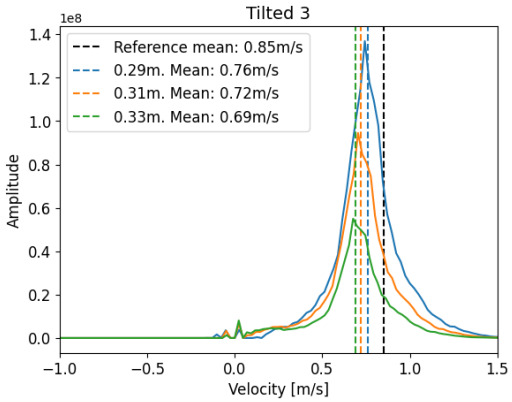

(c) Tilted 3, reference mean surface velocity of 0.85 m/s.

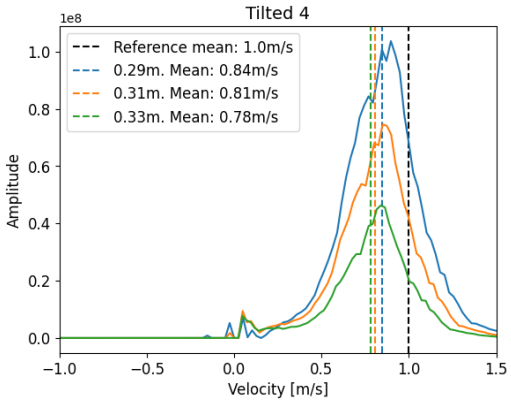

(d) Tilted 4, reference mean surface velocity of 1 m/s.

Figure 4.5: The plots show four different measurements (higher water flows due to increased inclination of the pipe). In each plot, the three distance points closest to the 45° angle distance, for each of the tilted pipes from figure 4.4. The reference mean surface velocity is measured to be ~ 0.5, 0.7, 0.85, and 1 m/s for the respective subplot.

We again see the increased velocities, but also the calculated mean average and the measured reference velocity as vertical lines. This reference should however not be considered the most reliable method, but still a good performance reference. During the measurement, the floating object was dropped in the middle of the flow, hence travelling with some of the higher velocity components rather than the slow ones. Note that the reference velocity deviates in the same direction for all measurements, i.e., the reference is slightly higher than the calculated mean average velocity. This data is also represented in the table 4.1 with the relative error to the estimated velocity made manually.

Table 4.1: A table over the estimated and obtained velocities in [m/s] together with a percentage of error in parenthesis for the data in figure 4.5.

	Ref velocity	d1	d2	d3
Tilted 1	0.5	0.45 (-10%)	0.41 (-18%)	0.34 (-32%)
Tilted 2	0.7	0.65 (-7%)	0.62 (-11%)	0.6 (-14%)
Tilted 3	0.85	0.76 (-11%)	0.72 (-15%)	0.69 (-19%)
Tilted 4	1.0	0.84 (-16%)	0.81 (-19%)	0.78 (-22%)

Figure 4.6 shows the measurement done for the same flow and settings, only having turned the sensor around, i.e., measuring the forward and backward flow. By Acconeer convention the forward flow is 'positive'. Figure 4.6a is the original result and in figure 4.6b the backward flow is mirrored in the y-axis centred around zero.

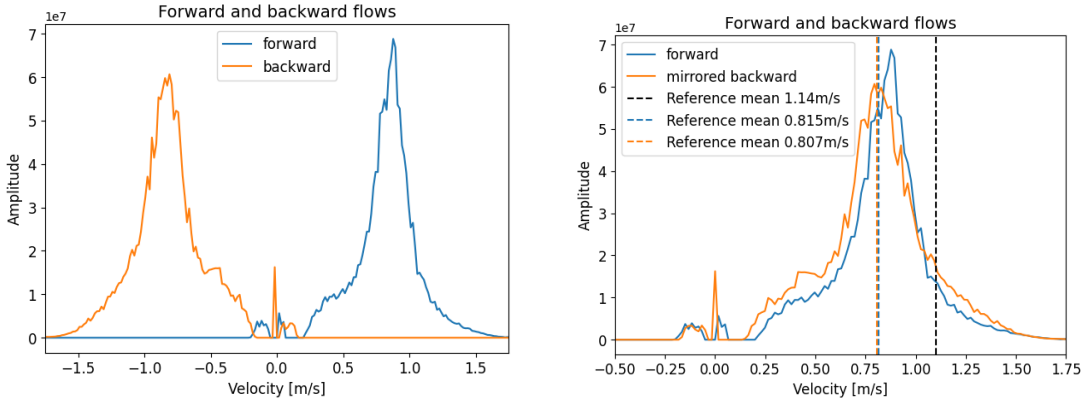

(a) Original data

(b) Mirroring the backward flow

Figure 4.6: The signal for the distance closest to the 45° angle for measurement forward and backward to the flow. The spectra are similar. The reference mean water surface velocity is measured to be ~ 1.1 m/s as shown in the vertical line.

The two measurements show similar spectra which are both centred around approximately the same mean velocity and has the same amplitude. The reference mean water surface velocity is measured to be ~ 1.1 m/s. From this, we see that the flowing direction is easy to determine. When mirroring these spectra in the x-axis as in figure 4.6b the PSD's are overlapping with approximately the same mean surface velocity. Assuming that the flow was constant and distributed in the same way within the pipe during the two measurements this is a satisfactory result. These results gives proof-of-concept in the area of measuring different flow directions. This is important for future further development. All of the results regarding correlation between flow velocity and flowing direction is important, and give the necessary basis for further implementation of the surface velocity algorithm for the A121 sensor.

4.2 UK lab environment

From the lab in UK, data from two different pipes were collected at two different occasions. Figures 4.7 - 4.11 are plots from 10 different flows from a rectangular pipe and the figures 4.12 - 4.16 from a circular pipe. All the measurements are done for the ~ 45° angle distance. In appendix, figures B.3 and B.4, the given data and pipe dimensions can be found together with the mean flow. The reader is reminded that the mean flow for the UK data is for the entire water flow, not just the surface. The plots are the mean over all 1000 frames and come in the order of increasing UK reference water velocity.

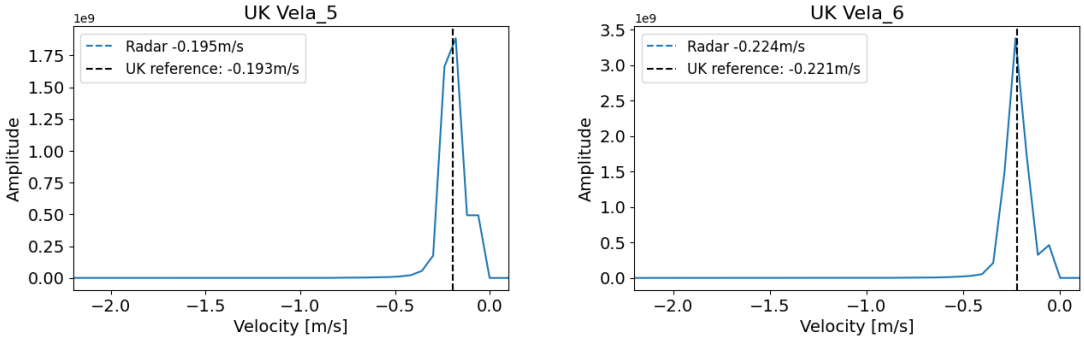

Figure 4.7: Data from the UK lab for rectangular pipe. Vertical line for the calculated mean value (from the data) and the UK reference (mean velocity for the entire water flow).

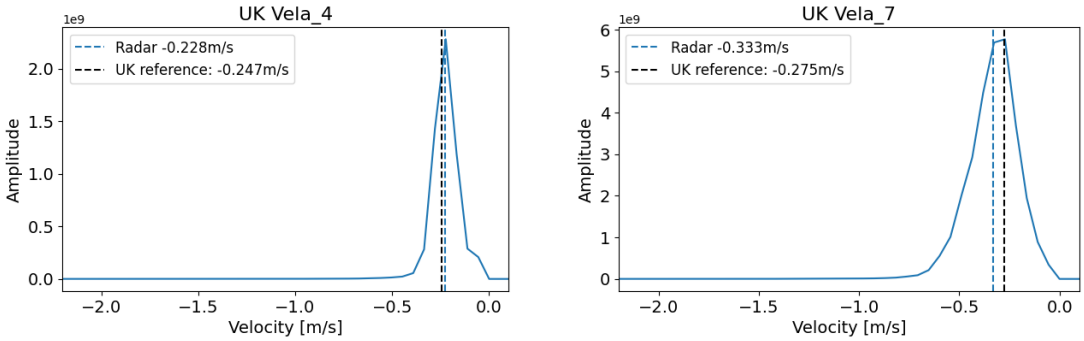

Figure 4.8: Data from the UK lab for rectangular pipe. Vertical line for the calculated mean value (from the data) and the UK reference (mean velocity for the entire water flow).

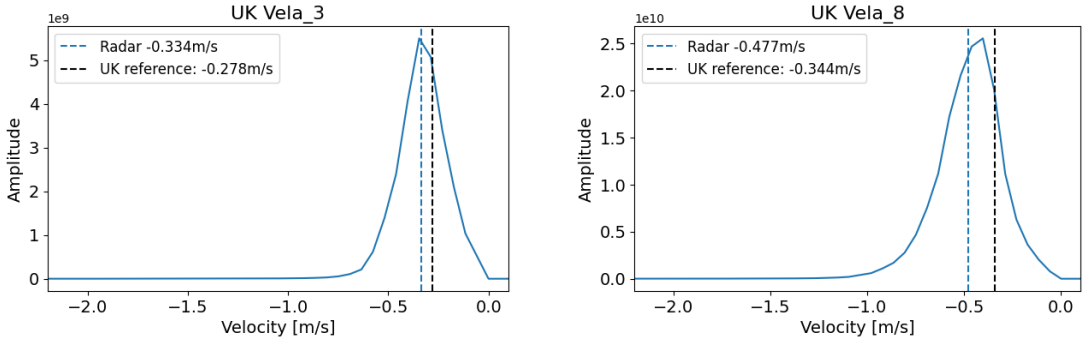

Figure 4.9: Data from the UK lab for rectangular pipe. Vertical line for the calculated mean value (from the data) and the UK reference (mean velocity for the entire water flow).

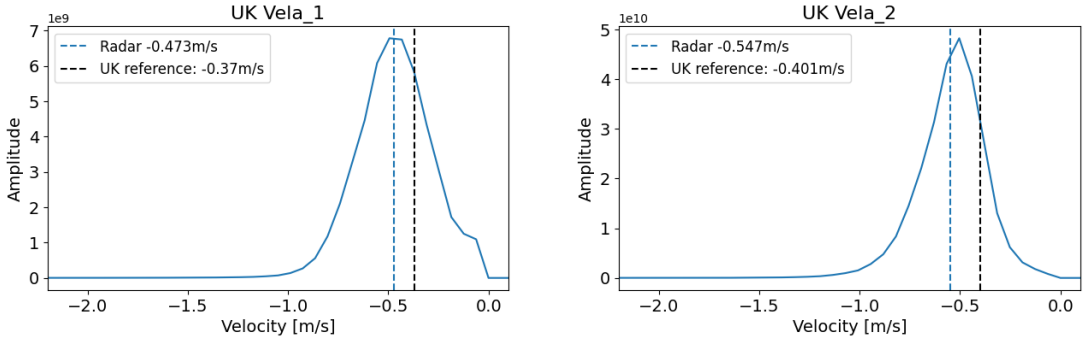

Figure 4.10: Data from the UK lab for rectangular pipe. Vertical line for the calculated mean value (from the data) and the UK reference (mean velocity for the entire water flow).

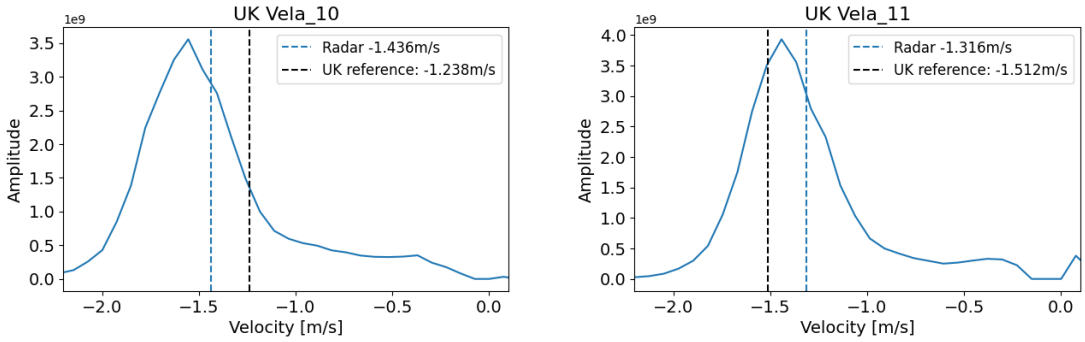

Figure 4.11: Data from the UK lab for rectangular pipe. Vertical line for the calculated mean value (from the data) and the UK reference (mean velocity for the entire water flow).

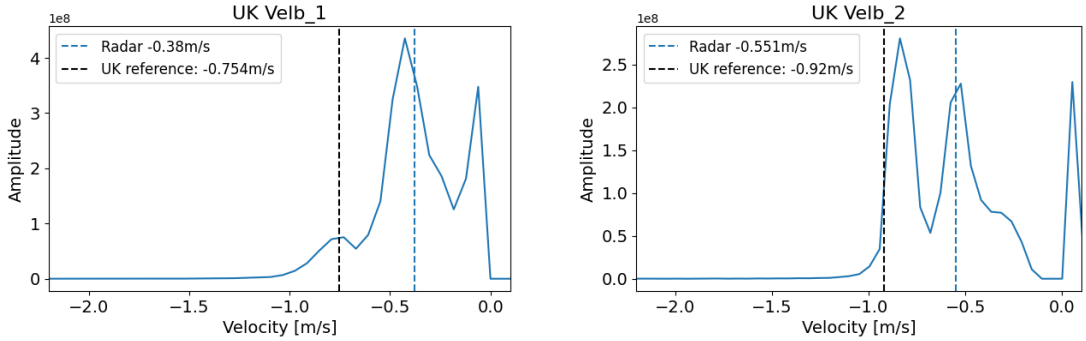

Figure 4.12: Data from the UK lab for circular pipe. Vertical line for the calculated mean value (from the data) and the UK reference (mean velocity for the entire water flow).

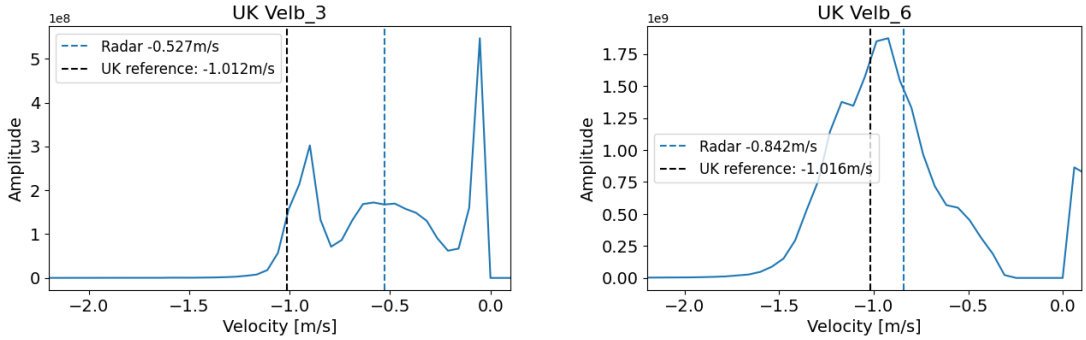

Figure 4.13: Data from the UK lab for circular pipe. Vertical line for the calculated mean value (from the data) and the UK reference (mean velocity for the entire water flow).

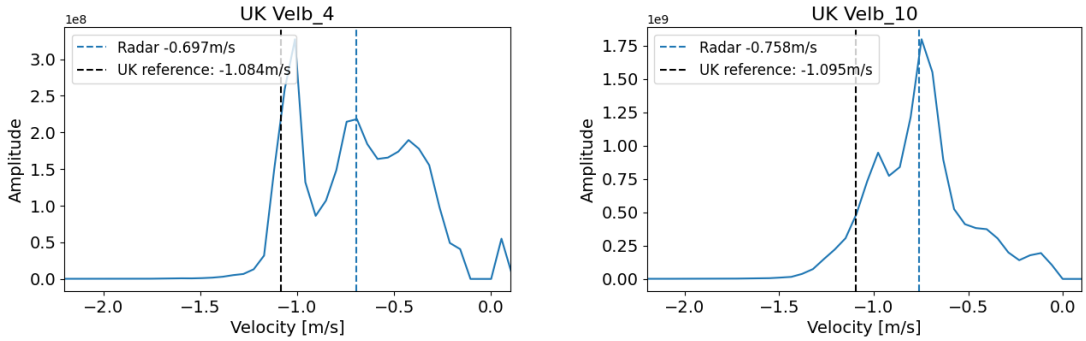

Figure 4.14: Data from the UK lab for circular pipe. Vertical line for the calculated mean value (from the data) and the UK reference (mean velocity for the entire water flow).

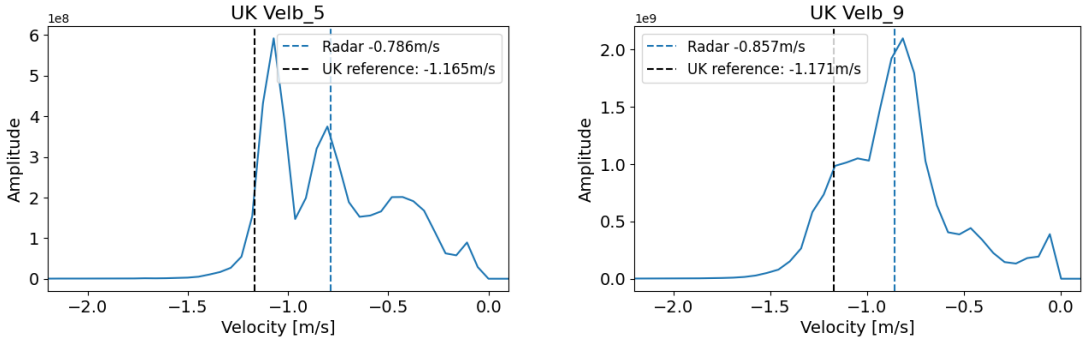

Figure 4.15: Data from the UK lab for circular pipe. Vertical line for the calculated mean value (from the data) and the UK reference (mean velocity for the entire water flow).

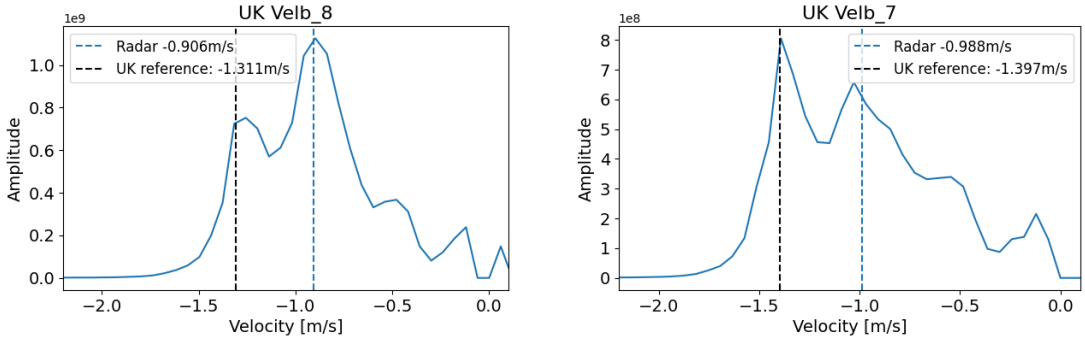

Figure 4.16: Data from the UK lab for circular pipe. Vertical line for the calculated mean value (from the data) and the UK reference (mean velocity for the entire water flow).

For the rectangular pipe measurements of figure 4.7 - 4.11, the radar generally predicts a higher mean surface velocity than the calculated average mean velocity. The spectra of these plots contain only one peak which is in accordance with the plots of figure 4.5a - 4.5d in section 4.1. For the circular pipe measurements of figure 4.12 - 4.16, the predictions of the mean surface velocity is significantly lower than the UK reference velocity and now multiple peaks are seen in the spectra. The results from the UK lab can be visualised in table 4.2 and table 4.3 respectively. The tables shows the mean velocity in [m/s] together with the error in comparison to the reference mean velocity.

Table 4.2: The table displays the mean reference velocity for all measurements from the rectangular pipe together with the calculated mean velocity from the sensor. All values are in [m/s] and in addition to the velocity the error to the reference is calculated in the parenthesis.

Name	Reference mean	All frames	
Vela1	0.370	0.473	(+28%)
Vela2	0.401	0.547	(+36%)
Vela3	0.278	0.334	(+20%)
Vela4	0.247	0.228	(-8%)
Vela5	0.193	0.195	(+1%)
Vela6	0.221	0.224	(+1%)
Vela7	0.275	0.333	(+21%)
Vela8	0.344	0.477	(+39%)
Vela10	1.238	1.436	(+16%)
Vela11	1.512	1.316	(-13%)

Table 4.3: The table displays the mean reference velocity for all measurements from the circular pipe together with the calculated mean velocity from the sensor. All values are in [m/s] and in addition to the velocity the error to the reference is calculated in the parenthesis.

Name	Reference mean	All frames	
Velb1	0.754	0.38	(-50%)
Velb2	0.920	0.551	(-40%)
Velb3	1.012	0.527	(-48%)
Velb4	1.084	0.697	(-36%)
Velb5	1.165	0.786	(-33%)
Velb6	1.016	0.842	(-17%)
Velb7	1.397	0.988	(-29%)
Velb8	1.311	0.906	(-31%)
Velb9	1.171	0.857	(-27%)
Velb10	1.095	0.758	(-31%)

Hence the rectangular pipe have a mean percentage error of +14% and the circular pipe have a mean error of -34% using all frames from the measurement.

Since the data presented in table 4.2 and 4.3 is the mean of all 1000 frames it is interesting to investigate any possible variation within these frames. Figures 4.17 - 4.20 show the variations for the slowest and fastest UK lab measurements for both the rectangular- and circular pipe. Each plot for 4 different 'frame windows' of 100 consecutive frames together with their mean velocity. Additionally, the mean velocity over frames (over time) is represented below the power spectra. Here, two dashed lines in green represents the 25% error to the reference to facilitate interpretation of the velocity results.

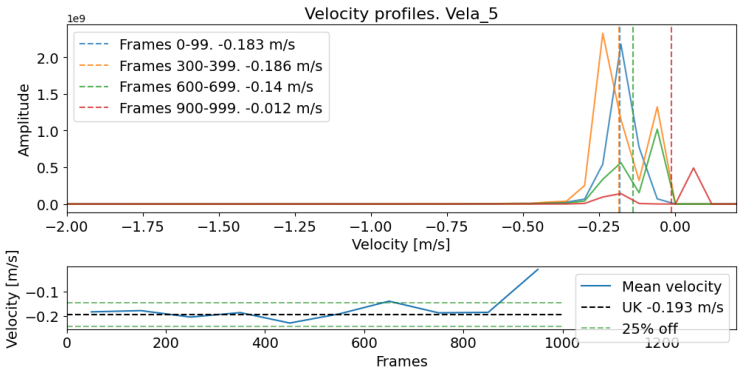

Figure 4.17: The frame variation of UK Vela 5 data (rectangular pipe). Both the power spectra and the mean velocity over frames.

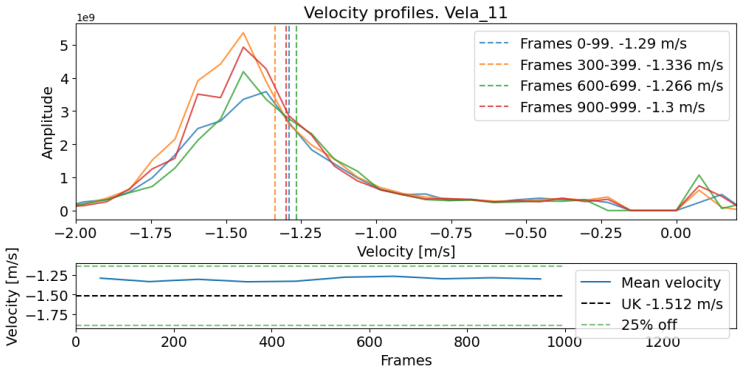

Figure 4.18: The frame variation of UK Vela 11 data (rectangular pipe). Both the power spectra and the mean velocity over frames.

The mean velocity of Vela_5 is alternating around the reference mean within the 25% error except for the for the last 100 frames. During this time the amplitude of the spectrum suddenly decreases causing the mean to go to zero which also can be seen in figure 4.17. According to figure 4.18, the flow velocity appears to be stationary with overlapping PSD's. The variations between the frame windows is small and the velocity is lower than the reference throughout the measurement.

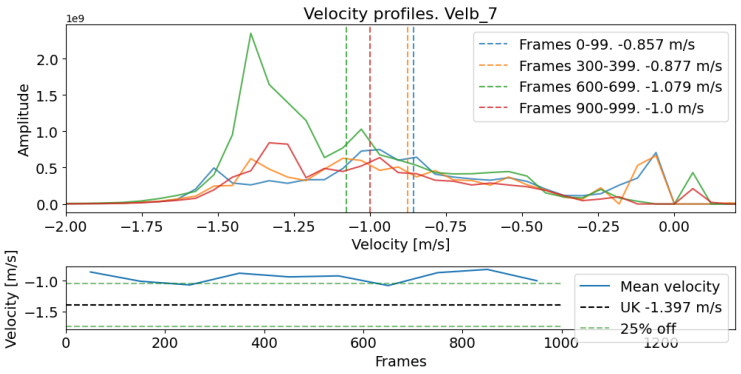

Figure 4.19: The frame variation of UK Velb 7 data (circular pipe). Both the power spectra and the mean velocity over frames.

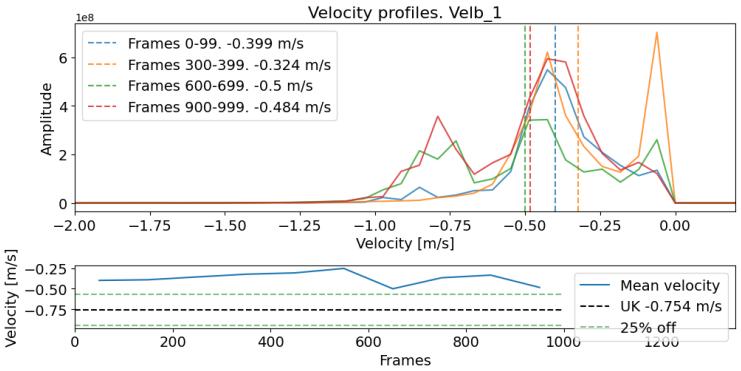

Figure 4.20: The frame variation of UK Velb 1 data (circular pipe). Both the power spectra and the mean velocity over frames.

Figure 4.19 show that the mean surface velocity is constantly lower than the reference mean and there is basically one frame window that differs significantly from the others (frames 600-699) with a PSD peak at ~1.4 m/s. Similarly, figure 4.20 show similar PSD with a mean velocity significantly lower than the reference mean. The PSD and hence the mean surface velocity may vary over time. There is a possibility that the water pump flow rate (which is set to a constant rate on the UK-pipe) vary over time or that the water level is not stationary which results in this time variation over different frames. For the rectangular pipe the mean surface velocity of the radar sensor increases as the reference increases. For the circular pipe it occurs multiple peaks. This is an odd phenomenon but since these measurements are done off-site it is hard to identify any specific sources of error. They may however arise due to some fluid dynamical 'fringe-formation'. We have higher velocities for the circular pipe than for the rectangular, seen in figures 4.7 - 4.16, which may cause a much more turbulent flow and hence irregularities in the surface ripples.

4.3 VA SYD site

The results of this segment are partitioned into the different sites where we have measured, namely `GYGK_K1500` (1500 mm), `TULK_750` (750 mm), and `TUAS_800` (800 mm). Data was collected on site at three different dates and is therefore named as measurement 1-3. For all results in this part there is an associated timestamp to all plots and the data is collected over one whole minute (corresponding to approximately 170 frames in this setting) before the timestamp. For example, 12:40 means that data is collected from 12:39:00-12:39:59. The reference velocity data of Nivus is for the last gate of the water layers, i.e., closest to the surface.

4.3.1 1500 mm

For the 1500 mm pipe, measurements were only conducted at one occasion. Figure 4.21 shows the power spectrum for three different timestamps and distances. In figure 4.22, the Nivus reference data is plotted for the same period and timestamps.

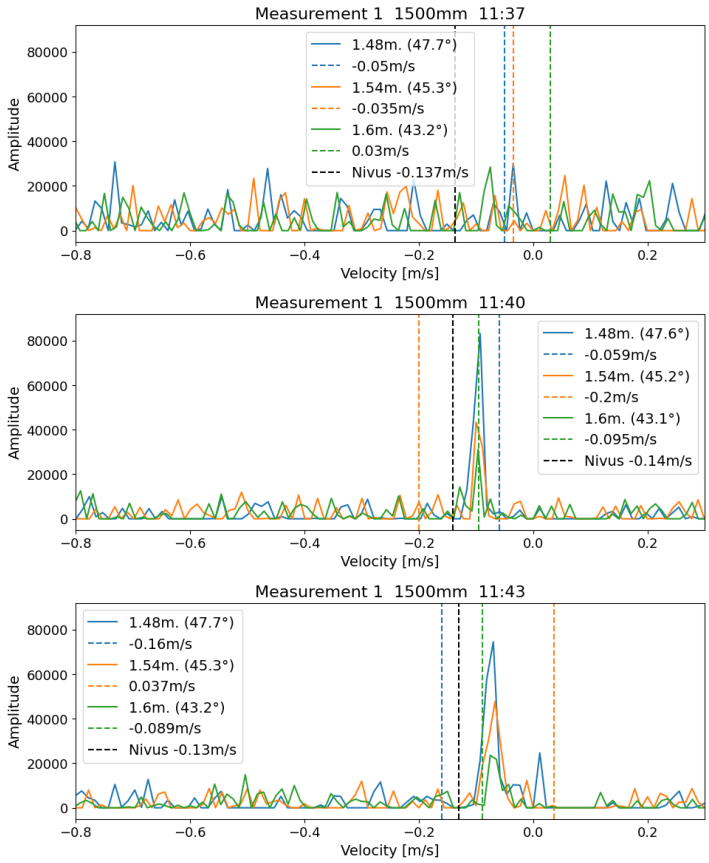

Figure 4.21: The power spectrum for the measurement on the 1500 mm pipe for three different timestamps. The different coloured spectra are for different distances. Vertical lines for mean value surface velocity and Nivus reference. The signal is noisy and has low amplitude, but for the second and third timestamp, there is a more prominent peak.

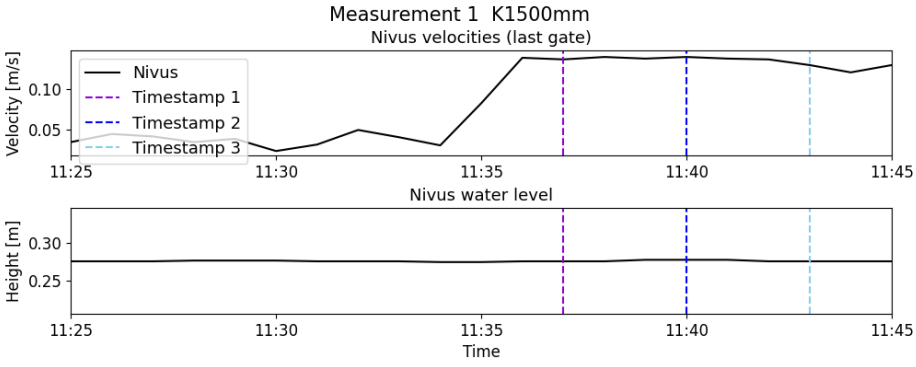

Figure 4.22: The Nivus last gate reference data for velocity (m/s) and water level. Vertical lines for the timestamps for data measuring plotted in figure 4.21. Note the increase in velocity at around 11:35.

As can be seen in figure 4.21 the reflected signal amplitude was low and the signal became noisy. This was caused by a smooth water flow with almost no ripples on the water surface. There is however some more protruding peaks for timestamps 11:40 and 11:43 around 0.09m/s which indicates that there is actually some surface velocity that is detected by the sensor. For further investigations it would be interesting to tilt the sensor down even further to receive stronger reflections. Looking at the velocities of figure 4.22 there is a sudden jump from ~0.03 m/s to ~0.14 m/s from 11:34 to 11:36 while constant water level. This was due to a manual cleaning of the sensor. The conclusion is that the Nivus reference system is in need of cleaning before measurement which was not done in all of the second measurements.

4.3.2 750 mm

Figure 4.23 and 4.25 shows the power spectrum for the first and second measurement on the 750 mm pipe for three different timestamps. The plots show spectra for three distances closest to the 45° angle distance with corresponding mean surface velocities as well as Nivus reference. Figure 4.24 and 4.26 shows the Nivus reference data for water velocity and water level in the 'last gate' for the three timestamps in figure 4.23 and 4.25 respectively.

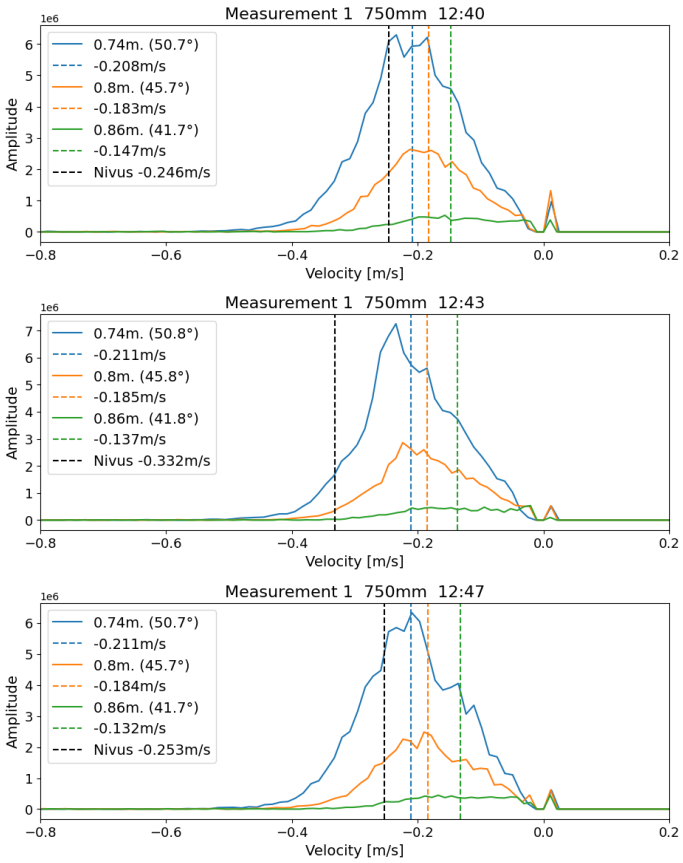

Figure 4.23: The power spectra for the first measurement on the 750 mm pipe for three different timestamps with corresponding mean value surface velocities as well as Nivus reference. The different coloured lines are for different distances, i.e., the ones closest to the 45° angle distance.

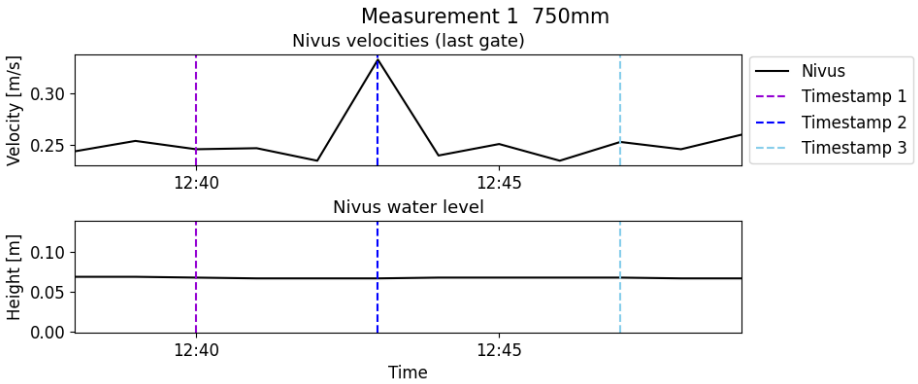

Figure 4.24: The Nivus reference data for water velocity and water level for the last gate of the water layers. The water level is somewhat constant, while the last gate velocity has a spike for timestamp 2.

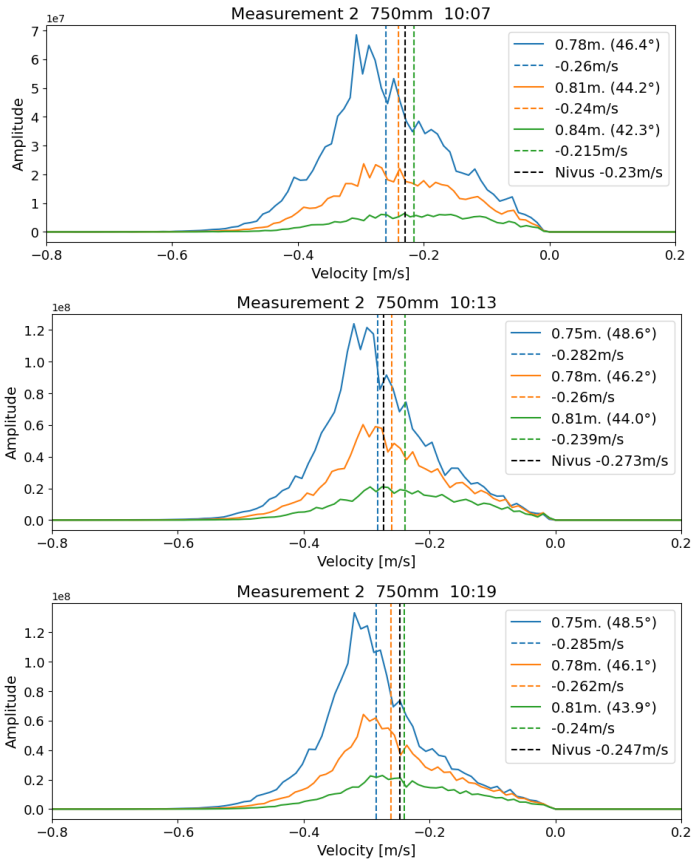

Figure 4.25: The power spectrum for the second measurement on the 750 mm pipe for three different timestamps with corresponding mean value surface velocities as well as Nivus reference. The different coloured lines are for different distances, i.e., the ones closest to the 45° angle distance.

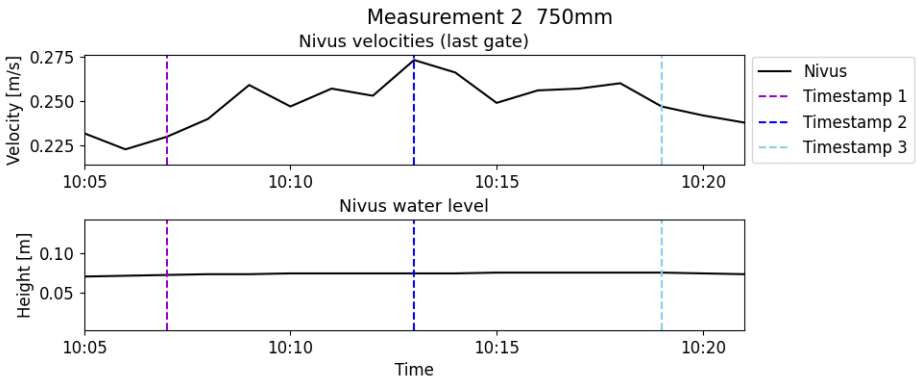

Figure 4.26: The Nivus reference data for the second measurement for water velocity and water level for the last gate of the water layers.

The PSD are distinct for both the first and second measurements, i.e., figure 4.23 and figure 4.25. During the first measurement it occurred a single peak at 12:43 where the velocity

spiked from 0.235 m/s to 0.332 m/s and then down to approximately the same velocity again. Analysing the PSD from our sensor in figure 4.23, indicates that this peak is some kind of measurement error for the reference data.

To get a better understanding of how the calculated mean velocity changes over time, figures 4.27 and 4.28 show the mean estimation and the Nivus reference last gate velocity over time for the three best distances for the respective measurements **1** and **2**.

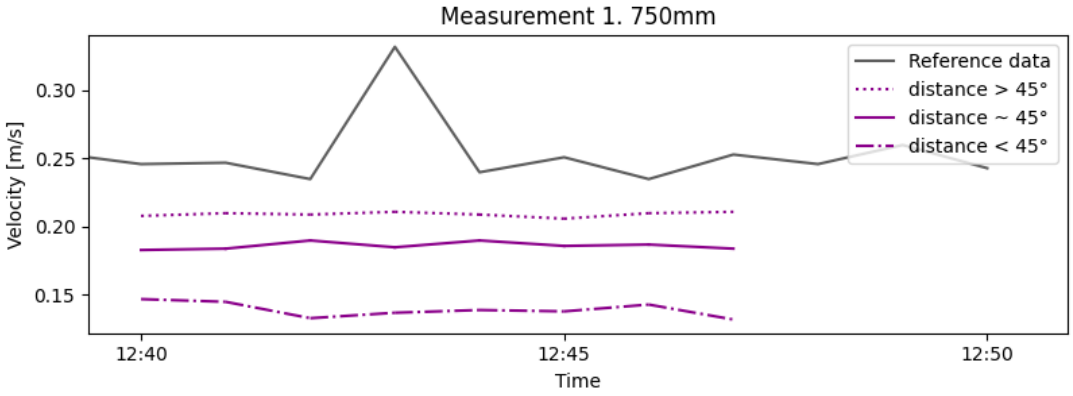

Figure 4.27: The Nivus reference last gate velocity and the calculated mean surface velocity over time for three different distances (closest to the 45° angle) during the first measurement. Nivus reference is consistently somewhat higher.

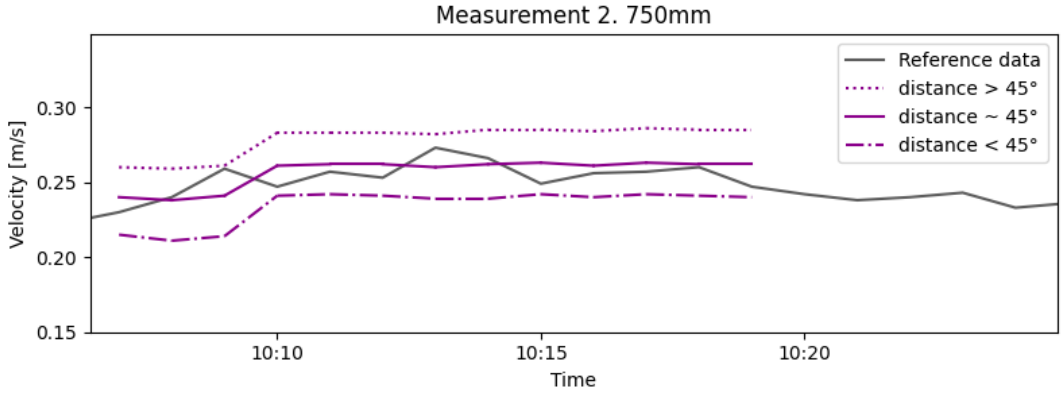

Figure 4.28: The Nivus reference last gate velocity and the calculated mean surface velocity over time for three different distances (closest to the 45° angle) during the second measurement.

The sensor spectrum averaged mean results in a constantly lower surface velocity than the reference data for the first measurement (figure 4.27) whereas for the second measurement the Nivus reference is much more in accordance with the calculated averaged mean (figure 4.25). Having a higher reference value is also seen for the Acconeer and UK lab plots, which are all for circular pipes. Looking back at figure 4.21 we see this phenomenon again,

the reference is slightly higher. However, for the second measurement of the 750 mm pipe the Nivus sensor was not cleaned, which may have caused a lower value of the velocity. The fact that we get a lower velocity is interesting and for the VA SYD measurements it is somewhat reasonable. The Nivus reference does not measure the surface but the last gate velocity, which should be slightly higher, in accordance to figure 2.15. However, for the Acconeer and UK lab environment it is fascinating and may be caused by some fluid dynamics of circular pipes. This effect could affect and potentially accentuate the off-set of VA SYD measurements.

4.3.3 800 mm

Figure 4.29 shows the power spectrum for the first measurement on the 800 mm pipe for three different timestamps for three distances. The corresponding mean value surface velocity as well as Nivus reference is showed as dashed lines. Figure 4.30 shows the Nivus reference data for water velocity and water level in the 'last gate', for the three timestamps in figure 4.29. Note that during first measurement the sensor measured forward flow.

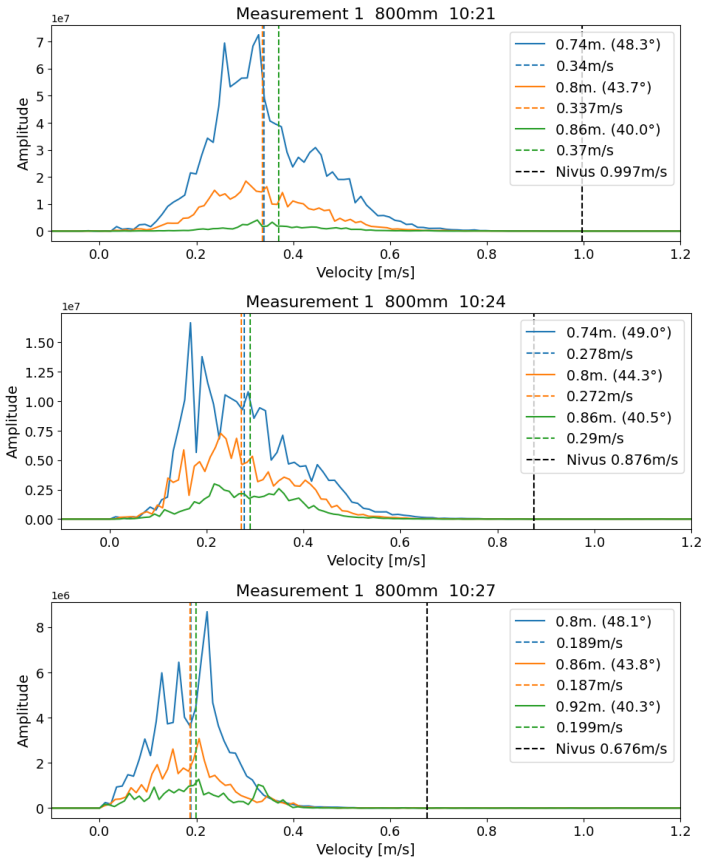

Figure 4.29: The power spectrum for the first measurement on the 800 mm pipe for three different timestamps. Also for three distances i.e., the ones closest to the 45° angle distance with vertical lines for mean value surface velocity and Nivus reference. Note that Nivus is much higher and outside our spectrum.

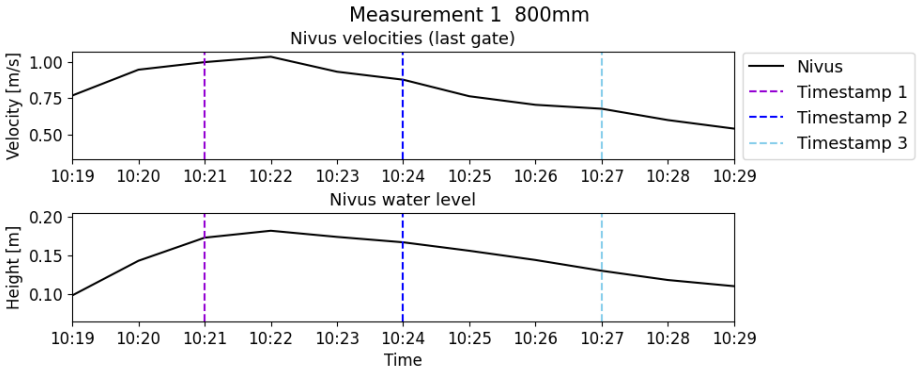

Figure 4.30: The Nivus reference data for the first measurement of the 800 mm pipe for water velocity and water level for the last gate of the water layers with dashed vertical lines for the three timestamps represented in figure 4.29

Figure 4.31 and figure 4.33 show the power spectrum for the second measurement on the 800 mm pipe for different timestamps with vertical lines for the mean value surface velocity as well as Nivus reference. Figure 4.32 shows the Nivus reference data for water velocity and water level in the 'last gate' for the the timestamps of figures 4.31 and 4.33. The second measurement was conducted measuring backward flow as seen in the plots.

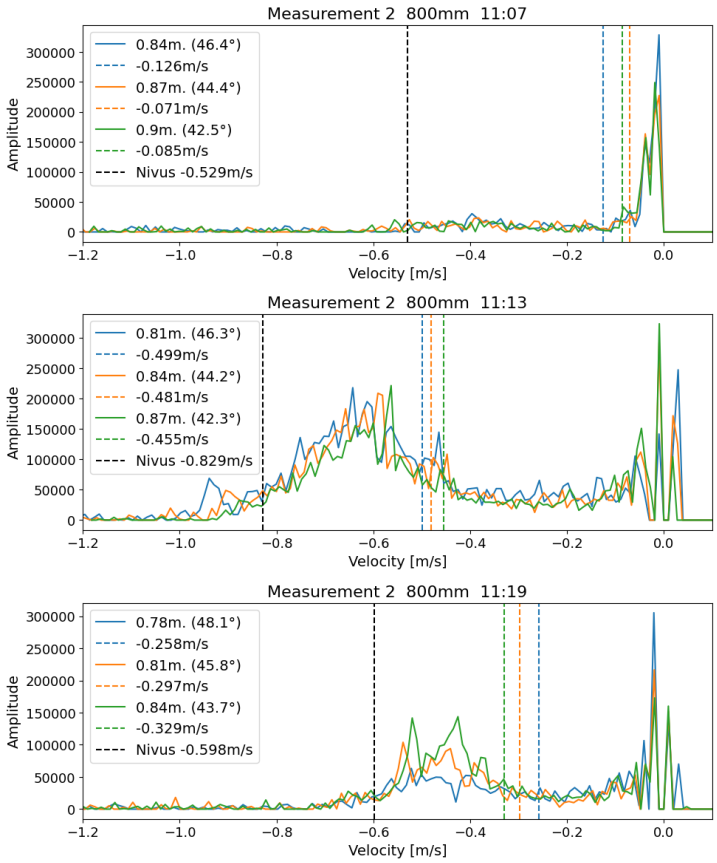

Figure 4.31: The power spectrum for the first second measurement on the 800 mm pipe for three different timestamps. The different coloured lines are for different distances, i.e., the ones closest to the 45° angle distance.

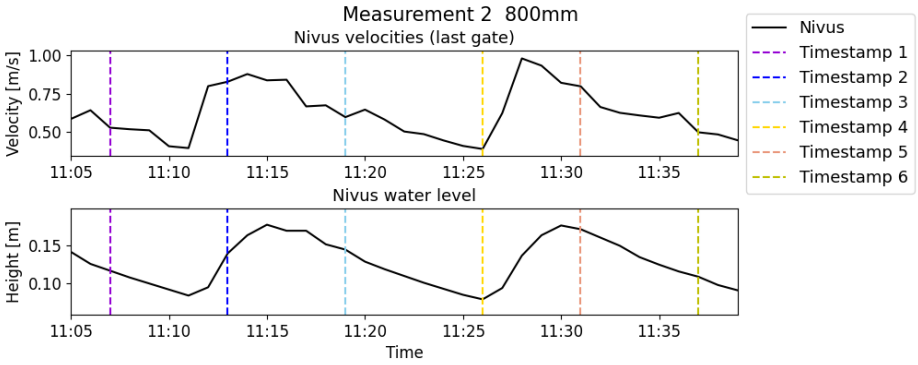

Figure 4.32: The Nivus reference data for the second measurement of the 800 mm pipe for water velocity and water level for the last gate of the water layers. The dashed vertical lines represent the timestamps represented in figures 4.31 - 4.33

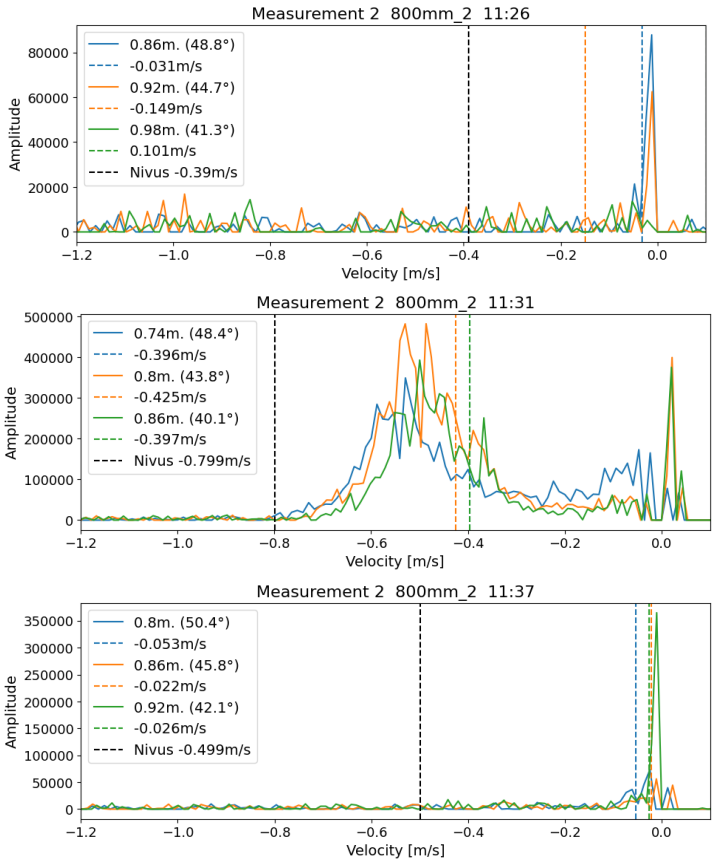

Figure 4.33: Power spectrum for the second measurement on the 800 mm pipe for three different timestamps. The different coloured lines are for different distances, i.e., the ones closest to the 45° angle distance. The vertical lines represent the mean value surface velocity and Nivus reference.

Due to the non-stationary flow of the `TUAS_800`, the sensor cleaned itself, hence missing the cleaning during the second measurement had less impact on the reference data. During measurement 1, i.e., figure 4.29, we get a relatively strong return signal and nice spectra. However, the Nivus reference is way off. During measurement 2, figure 4.31 and figure 4.33, only 11:13 has an 'acceptable' PSD peak that includes the reference velocity and 11:31 having a reasonable peak but outside the mean velocity. The other selected timestamps during this measurement results in a mean velocity close to zero since there is no signal strength with frequency content. For the timestamps during measurement 3 the signal strength was better than the first two times. With the timestamps in mind there seem to be some correlation between the water level and the received frequency content, sometimes there is no signal and suddenly there is a 'good' signal.

Measurements were made for a third time from this pipe as well, measuring backward flow. For figure 4.34 data were collected as before but for figure 4.36 the sensor was replaced with another sensor. Figure 4.35 represents the reference data with vertical lines for the Nivus reference data.

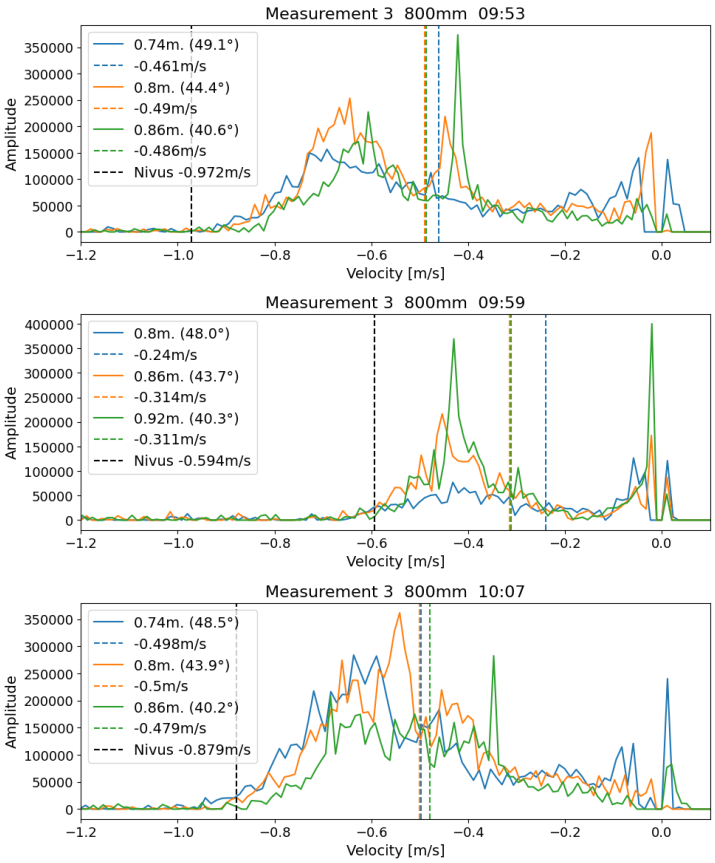

Figure 4.34: First third measurement (the old sensor) for three different timestamps. The signal strength is not that high. The different coloured spectra are for different distances, i.e., the ones closest to the 45° angle distance. Vertical lines represent mean value surface velocity and Nivus reference. Note that Nivus reference is much higher than calculated mean and outside spectrum.

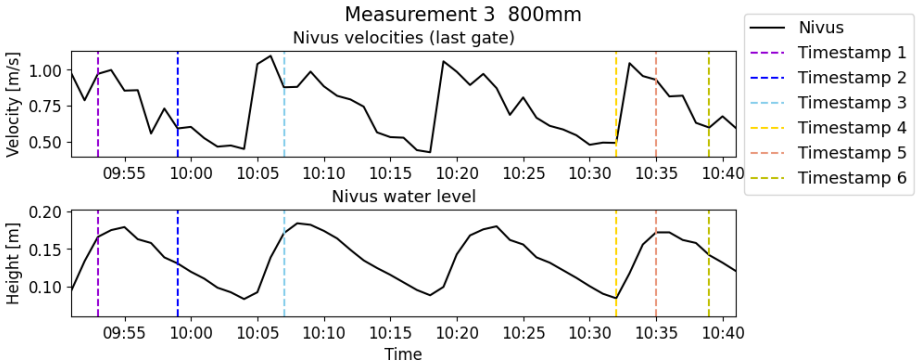

Figure 4.35: The Nivus reference data for last gate velocity and water level for the timestamps of figures 4.34 and 4.36.

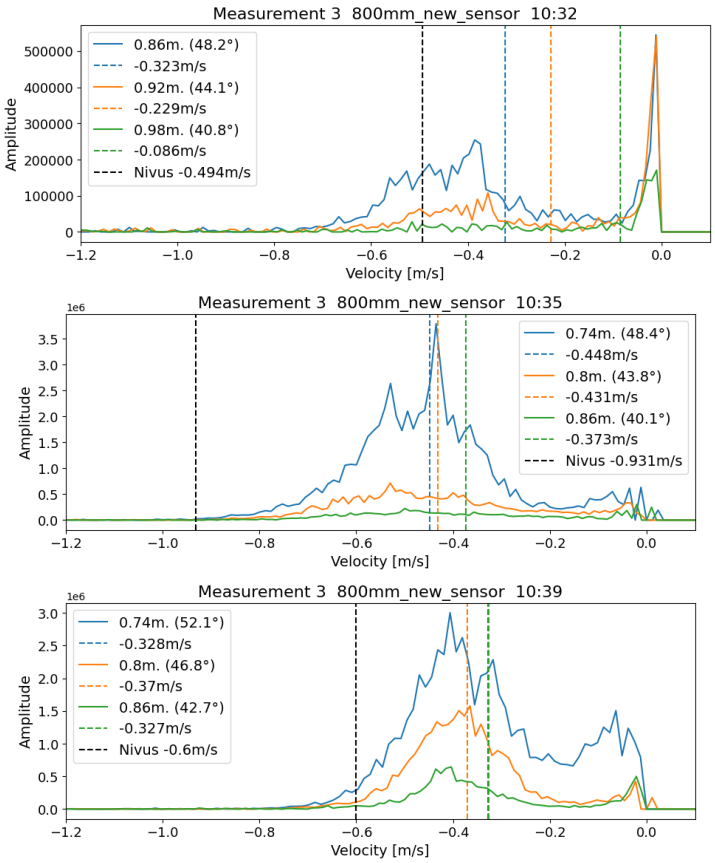

Figure 4.36: Second third measurement, i.e., with a new sensor, for three different timestamps. Again, the coloured spectra are for different distances, i.e., the ones closest to the 45° angle distance. Vertical lines represent mean value surface velocity and Nivus reference. The signal strength seems somewhat higher than in figure 4.34.

To get a better understanding of how the mean velocity changed over time, figures 4.37 - 4.39 show the calculated mean surface velocity and the Nivus last gate reference over time for the three best distances, i.e., closes to the 45° distance. For these plots the signal strength is also represented in different opacities (the signal strength refers to the the mean amplitude of the spectrum). As reference the PSD spectrum at 11:13 in figure 4.31 is set to be relatively good and therefore have a signal strength of 70% yielding that an amplitude mean of more than 40k counts as full signal strength. Note that the signal strength seem to weaken in the dips of the Nivus reference velocity. Looking at e.g. figure 4.35 we see that the last gate velocity periodically varies in sync with the water level.

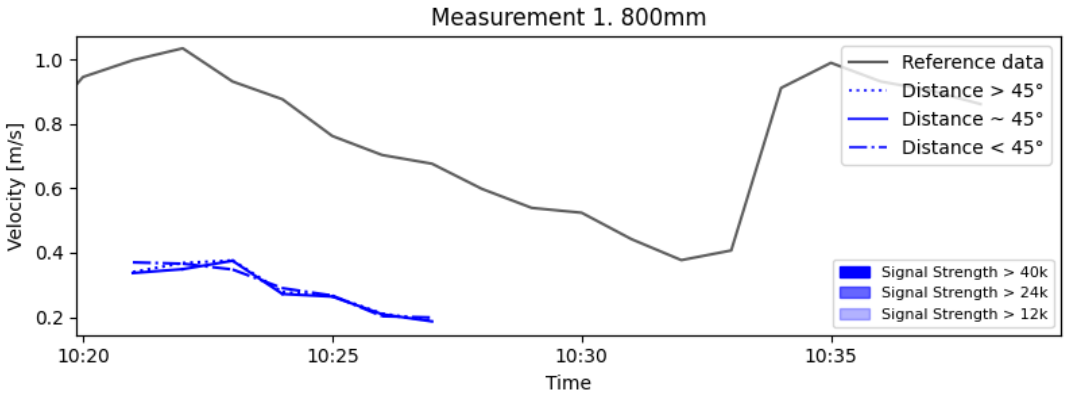

Figure 4.37: The calculated mean surface velocity and the Nivus last gate velocity over time for the first measurement. Plot is for three distances closest to the 45° angle distance. In this plot, opacity is taken as an argument to represent the signal strength of the return signal.

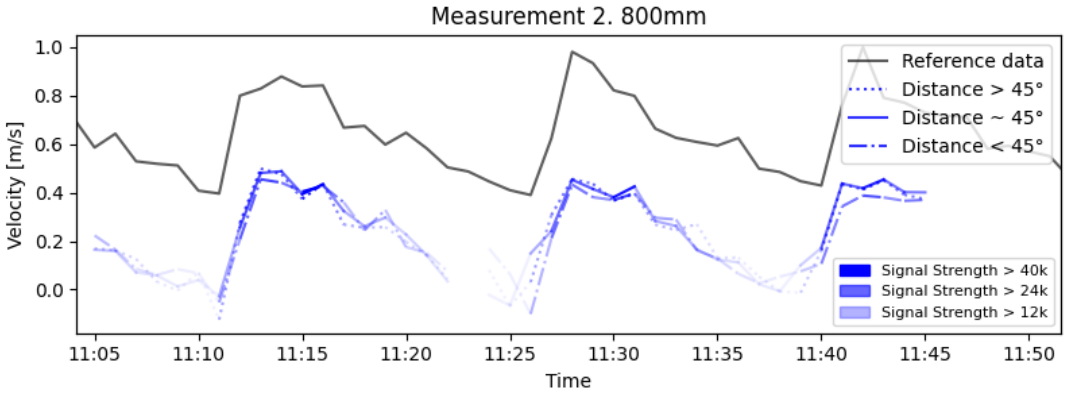

Figure 4.38: The calculated mean surface velocity and the Nivus last gate velocity over time for the second measurement. Plot is for three distances closest to the 45° angle distance. In this plot, opacity is taken as an argument to represent the signal strength of the return signal. The signal strength seem to weaken in the dips of the velocity (which coheres with a lower water level, seen for example in figure 4.35).

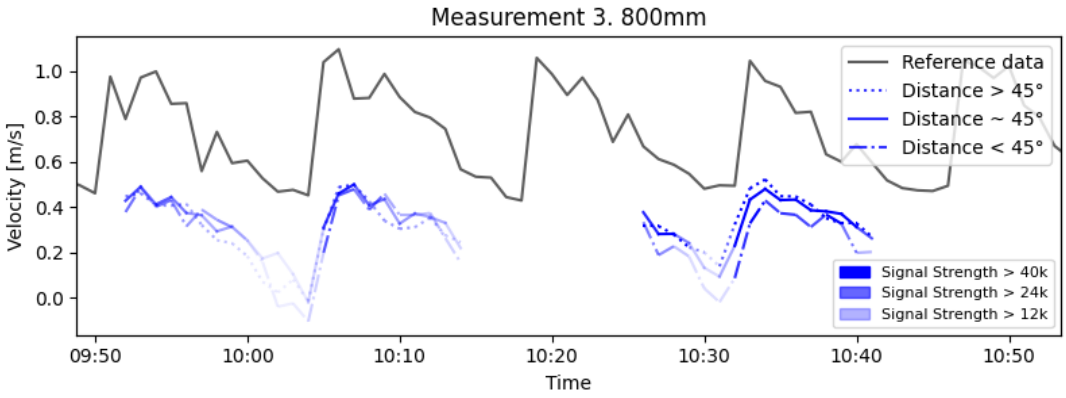

Figure 4.39: The calculated mean surface velocity and the Nivus last gate velocity over time for the third measurement. Plot is for three distances closest to the 45° angle distance. In this plot, opacity is taken as an argument to represent the signal strength of the return signal. The signal strength seem to weaken in the dips of the velocity (which coheres with a lower water level, seen for example in figure 4.35).

The change in return signal in relation to the non-stationary water levels are investigated in figures 4.37 - 4.39. The signal strength is best at the beginning of and during the peaks and decreasing during the 'slowdown' which eventually becomes noisy in the dips. Note that measurement 1 in figure 4.37 has a stronger return signal than then other measurements. This measurement was done with the forward flow. Looking at figure 4.39 after 10:30 we have a stronger return signal than before. These measurements were done with a new sensor which was installed. There is a possibility that the sensor angle was different at these times and possibly resulting in more signal received by the sensor compared to the other 800 mm measurements. For a different angle, the spectra should also be compensated with a different factor, possibly generating measurements more in accordance with Nivus reference, especially for the measurement 1 in figure 4.29. However, since the exact operation of the Nivus reference gauge is unknown, it is of course possible that Nivus measure way too high values. Another source of error could be the fluid dynamics of non-stationary water flows. Since measurement 1 has the best return signal and i.e., PSD it is also the possibility of some faulty sensor behaviour.

Chapter 5
Conclusions

This project set out to measure the surface velocity of a fluid using the Acconeer A121 pulsed coherent sensor with fast-time phase change of the pulsed wave. The complex valued data of the returned signal data is converted to the frequency domain. The results of the measurements are presented and discussed in section 4 above.

5.1 Summary

In this project, we implement an algorithm for converting the returned signal of the Acconeer A121 pulsed coherent radar sensor from a fluid surface into a mean velocity. The main goal is to determine proof-of-concept for measuring fluid flow surface velocities. As the result shows, a forward flow can easily be distinguished from a backward flow. This result is of great importance in the aspect of developing better infrastructure and supervision of e.g. sewage systems. If the vertical distance from sensor to surface is known, the result is independent of selected distance point and the PSD's are overlapping. Furthermore, there is a clear difference between flow velocities, as higher velocities shifts the velocity spectra towards higher velocities.

There seem to be a difference (estimated vs reference mean) between the circular and rectangular pipe, where the reference is higher for almost all measurements for the circular pipes and that the reference is lower for the rectangular pipe. This is interesting and a potential future topic research, in combination with deeper knowledge of fluid dynamics and application-specific implementation.

In order to detect surface velocities, the surface needs to have ripple-/wave formations in order to receive reflected signals. E.g. for the 1500 mm pipe, the return signal is weak in comparison to the noise. There is however some protruding peak which cohere with Nivus reference. For a pipe like this, specific algorithm and signal processing may be suitable.

5.2 Topical future research

Since the relation between the surface velocity and the mean velocity is both dependant on the pipe's shape and fluid level it would be interesting to combine the measured spectrum data with fluid dynamics of certain pipes. With deeper knowledge about fluid dynamics, one could find precise methods to convert the surface velocity measurement to fluid mean velocity.

For further investigations in this subject it would be interesting to see how the sensor angle affects the measurements. The angle-parameter is the trade-off between signal strength and measuring the horizontal component and maybe a steeper angle than 45°, especially for smooth flows like our 1500 mm pipe, would be beneficial.

Furthermore, assuming that the distance to the surface is correct and that there is more accurate data available there might be an optimal combination of different distances when converting to the mean surface velocity. For instance, having three distances, with angles $[47° \; 45° \; 42°]$ and corresponding mean velocities $[0.43 \; 0.55 \; 0.47]$ m/s weighting them together as,

$$V_{mean} = \begin{pmatrix} 0.25 & 0.5 & 0.25 \end{pmatrix} \begin{pmatrix} 0.43 \\ 0.55 \\ 0.47 \end{pmatrix} = 0.5 \, m/s \tag{5.1}$$

to gain more stability instead of just using one single distance. The variation between distances in the measurements might occur due to non exact measurements of sensor to water distance. Using a second non-interfering sensor with distance detection, one could obtain accurate sensor-to-water distance which would be beneficial.

For non-stationary flows it might be of interest to detect fast changes in velocity whereas in a more stationary large pipe it is more of interest to get an accurate mean velocity. For this purpose, specifically for the non-stationary case with fast changes is would be of interest to investigate how many frames is needed to calculate an accurate mean velocity or the possibility of a moving average over the frames. This part of slow-time (frame) averaging yields problems for rapid changes in surface velocity. For the 800 mm pipe this is especially noticeable, which is described in chapter 4. It would be of interest to examine how the measurements are affected by non-stationary flows like this, both velocity-/water height wise. For future adaptation there is room for tailoring the algorithms and the mean velocity conversion depending on signal strength, fluid dynamics and pipe dimensions, for instance some noise reduction technique for the 1500 mm pipe.

For further validation of the measurements it would be interesting to investigate some statistics of how the algorithm performs. With the method of e.g. Bootstrapping one could use random sampling from the statistical distribution in order to increase the sample space, i.e. reducing variance and introduce good confidence intervals of the data. This way one could increase the statistically significance of the proof-of-concept for the measurements.

References

[1] M. A. R. et al., *Principles of modern radar: Basic principles, Volume 1*. Institution of Engineering Technology, 2015.

[2] C. Wolff, *Coherence in Radar*. Available at https://www.radartutorial.eu/11.coherent/co05.en.html, accessed 2022-05-18.

[3] A. AB, *Introduction to Acconeer's sensor technology*. Available at https://developer.acconeer.com/download/introduction-to-acconeers-sensor-technology-pdf, accessed 2022-03-18.

[4] A. AB, *Acconeer Sparse service*. Available at https://docs.acconeer.com/en/latest/services/sparse.html, accessed 2022-03-18.

[5] A. AB, *Getting Started Guide Lens Evaluation Kit LH112/122/132*. Available at https://developer.acconeer.com/download/getting-started-guide-lenses-pdf/, accessed 2022-03-31.

[6] S. Engelberg, *Digital Signal Processing*. Springer-Verlag London Limited, 2008.

[7] M. N. S. S. K. Deergha Rao, *Digital Signal Processing; Theory and practice*. Springer Singapore, 2018.

[8] V. C. Chen, *The Micro-Doppler Effect in Radar*. ARTECH HOUSE, 2011.

[9] P. Anju, A. Bazil Raj, and C. Shekhar, "Pulse doppler processing - a novel digital technique," in *2020 4th International Conference on Intelligent Computing and Control Systems (ICICCS)*, pp. 1089–1095, 2020.

[10] D. D. Ludovic Cassan, Héléne Roux, *Velocity distribution in open channel flow with spatially distributed roughness*.

[11] Y. J. et al., *Analysis of the Velocity Distribution in Partially-Filled Circular Pipe Employing the Principle of Maximum Entropy*. PLoS ONE 11(3): e0151578. doi:10.1371/journal.pone.0151578, March 17, 2016.

[12] W. D. Kimura, *Electromagnetic Waves and Lasers (Second Edition)*. IOP Publishing, 2020.

[13] D. Griffiths, *Introduction to Electrodynamics*, ch. 9, p.367-380. Upper Saddle River, N.J: Prentice Hall, 1999, 4th edition.

[14] R. Fitzpatrick, *Reflection at a dielectric boundary*. Available at https://farside.ph.utexas.edu/teaching/em/lectures/node104.html, accessed 2022-04-06.

[15] A. S. Maths and Physics, *The Inverse Square Law for Electromagnetic Waves*. Available at https://astarmathsandphysics.com/o-level-physics-notes/254-the-inverse-square-law-for-electromagnetic-waves.html, accessed 2022-03-16.

Appendices

Appendix A
Electromagnetic Waves

A.1 Basics

Electromagnetic waves are composed of oscillating magnetic- (***B***) and electric fields (***E***) which are orthogonal to the propagating direction (often called k-vector) and is visualized in figure A.1 (12).

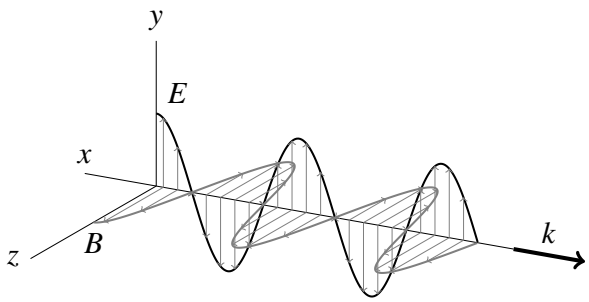

Figure A.1: The figure shows the EM wave where the magnetic field and electric field is orthogonal to both each other and to the k-vector respectively.

The most common wave equation is

$$f(z,t) = A\,cos[k(z - vt) + \delta] \tag{A.1}$$

where t represents time, z the distance in the propagating direction, A the amplitude of the wave. The argument of the cosine is called the phase and δ represents the phase shift (13).

The parameter k in equation A.1 is the wave number and can be expressed with the wave length λ as,

$$k = \frac{2\pi}{\lambda}. \tag{A.2}$$

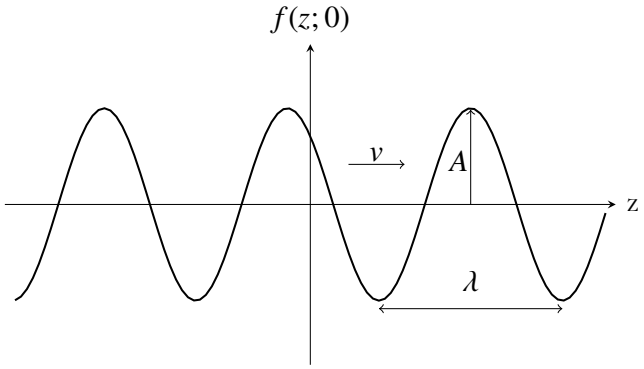

Figure A.2: The figure is an illustration of the simple cosine wave.

For a given point, letting the wave complete a full cycle is defined as a period,

$$T = \frac{2\pi}{kv} = \frac{\lambda}{v} \tag{A.3}$$

with a corresponding frequency

$$f = \frac{1}{T} = \frac{v}{\lambda} \tag{A.4}$$

which represents the number of oscillations per unit time (13).

Using the complex notation of $a + bj$ (for $j = \sqrt{-1}$ beeing the imaginary number) and Eulers formula, $e^{j\theta} = cos\theta + jsin\theta$, where θ denotes the argument, one can reformulate the wave from equation A.1 as

$$f(z,t) = Re[Ae^{j(kz-kvt)+\delta)}] \tag{A.5}$$

where Re denotes the real part of the complex wave.

A.2 Reflections and intensity

As mentioned before the EM-waves with a real frequency f can be written,

$$\begin{aligned} \boldsymbol{E}(\boldsymbol{r},t) &= E_0 e^{j(\boldsymbol{kr}-ft)}, \\ \boldsymbol{B}(\boldsymbol{r},t) &= B_0 e^{j(\boldsymbol{kr}-ft)} \end{aligned} \tag{A.6}$$

with amplitudes $\boldsymbol{E}_0$ and $\boldsymbol{B}_0$. Using the Maxwell equation,

$$\nabla \times \boldsymbol{E} = -\frac{\partial \boldsymbol{B}}{\partial t} \tag{A.7}$$

and knowledge about that the wave is transverse (meaning that $\boldsymbol{E}_0 \cdot \boldsymbol{k} = \boldsymbol{B}_0 \cdot \boldsymbol{k} = 0$) leads to the following relation between $\boldsymbol{E}_0$ and $\boldsymbol{B}_0$:

$$\boldsymbol{B}_0 = \frac{\hat{\boldsymbol{k}} \times \boldsymbol{E}_0}{v} \tag{A.8}$$

where $\hat{\boldsymbol{k}}$ denotes the unit vector pointing in the $\boldsymbol{k}$ (wave propagation) direction (14).

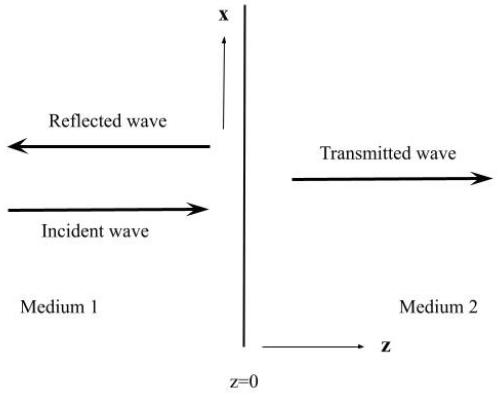

Figure A.3: The figure shows a schematic view over an electromagnetic wave perpendicular to a dielectric medium surface.

For a reflection of an incident wave perpendicular to a dielectric media we can express the waves as follows. Assuming that the incident wave is polarized in the x-direction it can be expressed as,

$$\begin{aligned} \boldsymbol{E}(z,t) &= E_i e^{j(\boldsymbol{k}_1 z - ft)}\hat{\boldsymbol{x}}, \\ \boldsymbol{B}(z,t) &= \frac{E_i}{v_1} e^{j(\boldsymbol{k}_1 z - ft)}\hat{\boldsymbol{y}} \end{aligned} \tag{A.9}$$

where $v_1 = \frac{c}{n_1}$ denotes the phase-velocity of the first medium and $k_1 = \frac{f}{v_1}$. n_1 is the refractive index and v_1 is the propagating speed of medium one. The reflected wave then becomes,

$$\begin{aligned} \boldsymbol{E}(z,t) &= E_r e^{j(-\boldsymbol{k}_1 z - ft)}\hat{\boldsymbol{x}}, \\ \boldsymbol{B}(z,t) &= -\frac{E_r}{v_1} e^{j(-\boldsymbol{k}_1 z - ft)}\hat{\boldsymbol{y}} \end{aligned} \tag{A.10}$$

and the transmitted wave takes the form,

$$\begin{aligned} \boldsymbol{E}(z,t) &= E_t e^{j(\boldsymbol{k}_2 z - ft)}\hat{\boldsymbol{x}}, \\ \boldsymbol{B}(z,t) &= -\frac{E_t}{v_2} e^{j(\boldsymbol{k}_2 z - ft)}\hat{\boldsymbol{y}} \end{aligned} \tag{A.11}$$

with $v_2 = \frac{c}{n_2}$and $k_2 = \frac{f}{v_2}$ for the second medium.

Having a normal incident like in figure (A.3) (assuming that both medias are non-magnetic) result in that both components of all the three waves are parallel yielding boundary conditions at z=0 which result in

$$E_i + E_r = E_t \tag{A.12}$$

for the electric components and

$$\frac{E_i - E_r}{v_1} = \frac{E_t}{v_2} \Leftrightarrow E_i - E_r = \frac{v_1}{v_2} E_t \tag{A.13}$$

for the magnetic components. Using these two equations (A.12 and A.13) together with the knowledge about that $\frac{v_1}{v_2} = \frac{n_1}{n_2}$ we end up at

$$\begin{aligned} E_r &= \left(\frac{n_1 - n_2}{n_1 + n_2}\right) E_i \\ E_t &= \left(\frac{2n_1}{n_1 + n_2}\right) E_i \end{aligned} \tag{A.14}$$

which represent the amplitude of the reflected and transmitted waves as a function of the incoming wave. The mean intensity in the z-direction (from figure A.3) is,

$$I = \frac{\langle \boldsymbol{E} \times \boldsymbol{B}\hat{\boldsymbol{z}} \rangle}{\mu_0} = \frac{E_0 B_0}{2\mu_0} = \frac{E_0^2}{2\mu_0 v}. \tag{A.15}$$

The coefficient of reflection (R) and coefficient of transmission (T) which is defined as the ratio of the reflected/transmitted and the incident wave respectively are derived from equation A.14 and becomes,

$$R = \frac{I_r}{I_i} = \left(\frac{E_r}{E_i}\right)^2 = \left(\frac{n_1 - n_2}{n_1 + n_2}\right)^2 \tag{A.16}$$

and

$$T = \frac{I_t}{I_i} = \frac{n_2}{n_1}\left(\frac{E_t}{E_i}\right)^2 = \frac{n_2}{n_1}\left(\frac{2n_1}{n_1 + n_2}\right)^2 \text{ (14)}. \tag{A.17}$$

Different frequencies gives different refractive indices for the same material and this is called chromatic dispersion. According to Acconeer, their 60 GHz radar have the approximated values for the real part of the relative permittivity and corresponding coefficient of reflections for different materials as represented in table A.1 (3). The relative permittivity is converted to a refractive index as $Re(\sqrt{\epsilon}) = Re(n)$ and can be found in the table as well.

Table A.1: Relative permittivity of common materials

Material	Real(ϵ)	Real(n)	R with air boundary
ABS plastic	2.48	1.57	0.0049
Concrete	4	2	0.11
Water	11.1	3.33	0.28
Air	1	1	0

Note that $T + R = 1$ and therefore all all energy which is not transmitted at the boundary is then reflected. However the intensity of an EM-wave in space can be described through the inverse square law since it is defined as the energy crossing per second per unit area. Assuming a spread in every spatial direction (from a point source), the intensity at any point on the surface of the sphere becomes

$$I = \frac{I_0}{4\pi r^2} \quad [W/m^2] \tag{A.18}$$

where r is the distance from the source to the sphere surface (15). The intensity of the wave thus decreases with $\propto 1/r^2$.

Appendix B
Tables and images

As seen in figures B.6 and B.7 the HBL and FZP lens limits the signal more in the angular E-plane and H-plane as well as increases the max gain [dB_{FS}]. The D2 lens setting, i.e., when placing the lens further away from the sensor, increases the gain and focuses the signal more than D1.

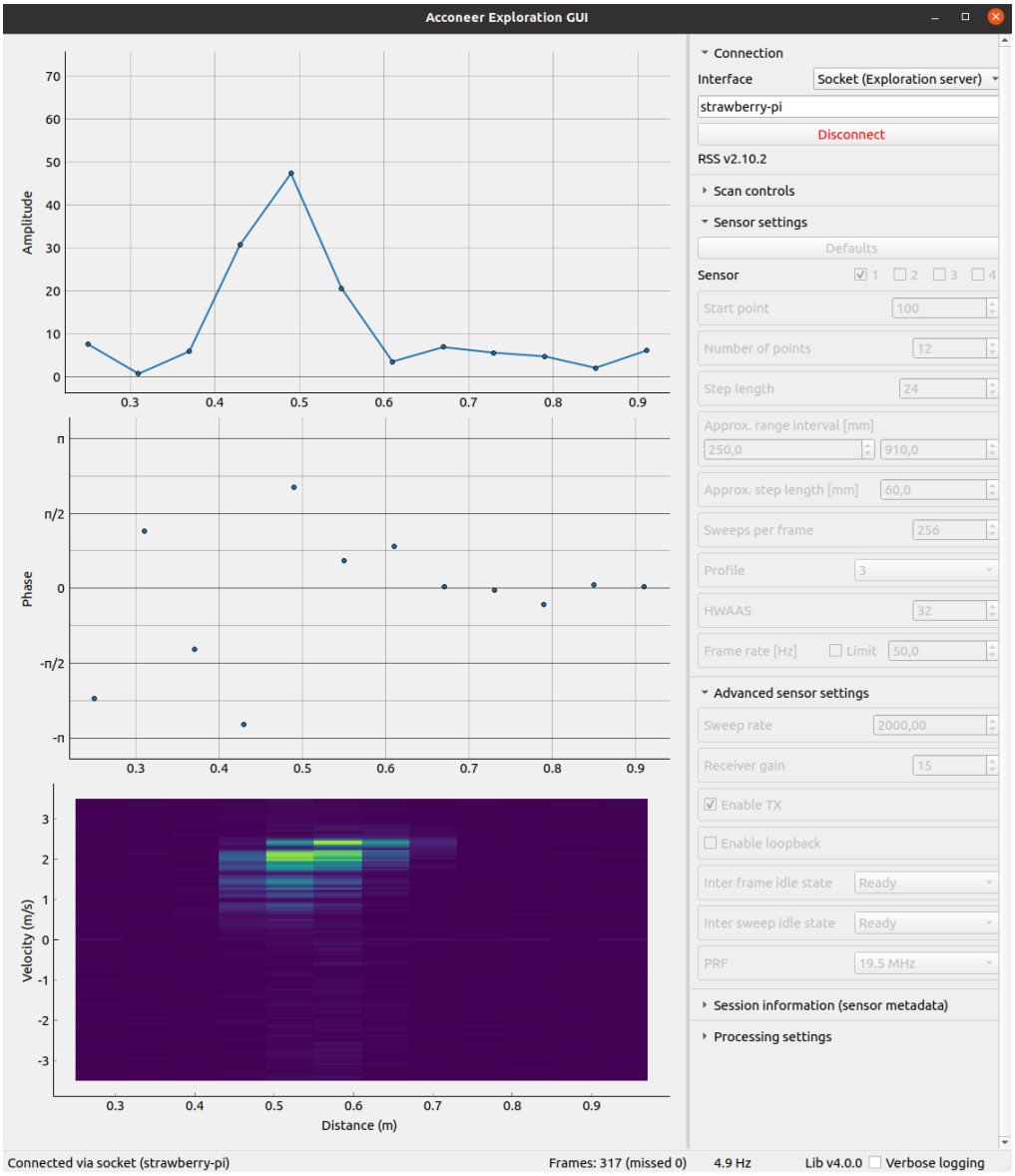

Figure B.1: The figure shows a Screenshot of the Sparse IQ GUI where all parameters can be set together with a visualization over the received signal.

```python

import numpy as np
from scipy import signal
import matplotlib.pyplot as plt

w_1 = 30 # frequency of the 1st component of the signal (Hz)
w_2 = 50 # frequency of the 2nd component of the signal (Hz)

a = 1.1 # magnitude of the 1st component of the signal
b = 0.6 # magnitude of the 2nd component of the signal

t = np.array([i for i in range(1,301)])/1000 # time samples (s)
fs = 1 / (t[1]-t[0]) # sampling frequency (Hz)

x = a*np.cos(2*np.pi*w_1*t) + b*np.sin(2*np.pi*w_2*t) # considered signa
f, Pxx_den = signal.periodogram(x, fs=fs, scaling='spectrum')

plt.subplots(1, 1, figsize=(6, 4), dpi=250)
plt.stem(f[:50], Pxx_den[:50], '-')
plt.ylabel('Spectrum')
plt.xlabel('Frequencies (Hz)')
plt.title('Periodogram')
plt.grid(True)
plt.show()

```

Figure B.2: The Python code used to generate the simple periodogram plot of figure 2.13.

Channel width	294	mm		
File name	Flow rate (l/s)	Depth (mm)	Wetted area (m^2)	Average velocity (m/s)
VelA_1	6,52	60	0,018	0,370
VelA_2	6,48	55	0,016	0,401
VelA_3	6,53	80	0,024	0,278
VelA_4	6,53	90	0,026	0,247
VelA_5	6,53	115	0,034	0,193
Average flow_1 (l/s)	6,518			
VelA_6	8,07	124	0,036	0,221
VelA_7	8,09	100	0,029	0,275
VelA_8	8,1	80	0,024	0,344
VelA_10	8,01	22	0,006	1,238
VelA_11	8	18	0,005	1,512
Average flow rate_2 (l/s)	8,05			
Distance of centre of Lens above base of channel =	45.5 cm			
Transducer angle =	45°			

Figure B.3: The received reference velocity data from UK for the rectangular pipe.

Pipe diameter	150	mm	pipe radius	75	mm
File name	Flow rate (l/s)	Depth (mm)	Theta Rads	Wetted area (m^2)	Velocity (m/s)
Velb_1	4,1	52	2,518214707	0,00544	0,754
Velb_2	4,1	45	2,318558961	0,00446	0,920
Velb_3	4,1	42	2,230395307	0,00405	1,012
Velb_4	4,1	40	2,170556409	0,00378	1,084
Velb_5	4,1	38	2,109757198	0,00352	1,165
Velb_6	5,24	50	2,461918835	0,00516	1,016
Velb_7	7,8	53	2,546169264	0,00558	1,397
Velb_8	7,7	55	2,601727062	0,00587	1,311
Velb_9	7,73	60	2,738876812	0,00660	1,171
Velb_10	7,71	63	2,820211348	0,00704	1,095
Average flow rate_2 (l/s)	7,74				
Distance of centre of Lens above base of channel =	30.5 cm				
Transducer angle =	45°				

Figure B.4: The received reference data from UK for the circular pipe.

Figure B.5: The setup while measuring the surface flow velocity with slow motion camera and the Apple Watch in the Acconeer lab environment.

XR112 with LH112 holder	Max. Gain (dB_{FS})*		HPBW-E (degree)		HPBW-H (degree)	
	D1	D2	D1	D2	D1	D2
HBL	10.8	19	15	12	20	12
FZP	11.2	17	25	12	12	10

Figure B.6: The performance table of the LH112 mount holder and HBL/FZP lens (5).

XM122 with LH122 holder	Max. Gain (dB_{FS})*		HPBW-E (degree)**		HPBW-H (degree)**	
	D1	D2	D1	D2	D1	D2
HBL	11.4	19	22	17	30	15
FZP	12	15.2	20	12	27	12

Figure B.7: The performance table of the LH122 mount holder and HBL/FZP lens (5).